A Numerical Study of Nonlinear Nonhydrostatic Conditional Symmetric Instability in a Convectively Unstable Atmosphere

CHARLES J. SEMAN

Department of Atmospheric and Oceanic Sciences, University of Wisconsin—Madison, Madison, Wisconsin

(Manuscript received 11 September 1991, in final form 8 September 1993)

ABSTRACT

Nonlinear nonhydrostatic conditional symmetric instability (CSI) is studied as an initial value problem using a two-dimensional (y, z) nonlinear, nonhydrostatic numerical mesoscale/cloud model. The initial atmosphere for the rotating, baroclinic (BCF) simulation contains large convective available potential energy (CAPE). Analytical theory, various model output diagnostics, and a companion nonrotating barotropic (BTNF) simulation are used to interpret the results from the BCF simulation. A single warm moist thermal initiates convection for the two 8-h simulations.

The BCF simulation exhibited a very intricate life cycle. Following the initial convection, a series of discrete convective cells developed within a growing mesoscale circulation. Between hours 4 and 8, the circulation grew upscale into a structure resembling that of a squall-line mesoscale convective system (MCS). The mesoscale updrafts were nearly vertical and the circulation was strongest on the baroclinically cool side of the initial convection, as predicted by a two-dimensional Lagrangian parcel model of CSI with CAPE. The cool-side mesoscale circulation grew nearly exponentially over the last 5 h as it slowly propagated toward the warm air. Significant vertical transport of zonal momentum occurred in the (multicellular) convection that developed, resulting in local subgeostrophic zonal wind anomalies aloft. Over time, geostrophic adjustment acted to balance these anomalies. The system became warm core, with mesohigh pressure aloft and mesolow pressure at the surface. A positive zonal wind anomaly also formed downstream from the mesohigh.

Analysis of the BCF simulation showed that convective momentum transport played a key role in the evolution of the simulated MCS, in that it fostered the development of the nonlinear CSI on mesoscale time scales. The vertical momentum transport in the initial deep convection generated a subgeostrophic zonal momentum anomaly aloft; the resulting imbalance in pressure gradient and Coriolis forces accelerated the meridional outflow toward the baroclinically cool side, transporting zonal momentum horizontally. The vertical (horizontal) momentum transport occurred on a convective (inertial) time scale. Taken together, the sloping convective updraft/cool side outflow represents the release of the CSI in the convectively unstable atmosphere. Further diagnostics showed that mass transports in the horizontal outflow branch ventilated the upper levels of the system, with enhanced mesoscale lifting in the core and on the leading edge of the MCS, which assisted in convective redevelopments on mesoscale time scales. Geostrophic adjustment acted to balance the convectively generated zonal momentum anomalies, thereby limiting the strength of the meridional outflow predicted by CSI theory. Circulation tendency diagnostics showed that the mesoscale circulation developed in response to thermal wind imbalances generated by the deep convection.

Comparison of the BCF and BTNF simulations showed that baroclinicity enhanced mesoscale circulation growth. The BTNF circulation was more transient on mesoscale time and space scales. Overall, the BCF system produced more rainfall than the BTNF.

Based on the present and past work in CSI theory, a new definition for the term "slantwise convection" is proposed.

1. Introduction

The pioneering work on conditional symmetric instability (CSI) work was performed by Bennetts and Hoskins (1979), who showed that moist convective circulations could occur in a saturated, baroclinic atmosphere even though it contained no convective available potential energy (CAPE). The modeled CSI circulations were found to be unstable if the wet-bulb potential temperature surfaces were more vertical than the absolute vorticity vector (negative wet-bulb potential vorticity). Using a circulation integral approach, they predicted that the slantwise updrafts would be narrow and intense and slope up the wet-bulb potential temperature surfaces, with broad, weaker downdrafts.

Emanuel (1983a) used a two-dimensional Lagrangian parcel model to extend the theory further. Under the limit of convectively neutral conditions (moist adiabatic sounding), he found that the updrafts were tilted 45° from the vertical with growth rates proportional to the vertical wind shear. The slantwise convective avail-

Corresponding author address: Dr. Charles J. Seman, Geophysical Fluid Dynamics Laboratory, Princeton University, P.O. Box 308, Princeton, NJ 08542.

able potential energy associated with the baroclinic shear [SCAPE, Emanuel (1983b)] provided the energy source for the slantwise convection in this case. Emanuel also hypothesized that the baroclinically cool-side circulation would dominate, and that it may become frontogenetically enhanced in the inflow to the warm side of the original updraft.

Xu (1986) extended the theory of Bennetts and Hoskins (1979) by solving the linearized eigenvalue problem and found that the updrafts were narrow and intense, while the broad downdrafts were weaker, in agreement with their theory. He also showed that more CAPE, weaker symmetric stability (lower Ri), and weaker static stability favor increased growth of the mesoscale circulations. Additionally, he found that viscosity markedly reduces the growth rates.

The linear wave–CISK approach used by Emanuel (1982), Sun (1984), and Nehrkorn (1986) supported the growth rate results from CSI theory, and additionally predicted that the mesoscale circulations should propagate towards the warm air. The results are in general agreement with observations. However, as pointed out by Nehrkorn, the predicted growth rates (phase speeds) of the circulations are too small (large) to account for the observed characteristics of squall line–type mesoscale convective systems.

In earlier related work on the interaction between deep convection and its larger mesoscale environment, Emanuel (1980) showed that the mesoscale circulations associated with deep convection can be enhanced as the ambient symmetric stability (potential vorticity) is reduced. If the secondary circulations are hydrostatic and isentropic, the amount of work that must be done against the environment for an incremental fluid displacement δy is given by (Emanuel 1980)

$$\delta W = \frac{f^2}{\mathrm{Ri}}(1 - S)(\delta y)^2, \tag{1}$$

where the symmetric stability parameter is defined as

$$S = \frac{\eta}{f}\mathrm{Ri} \tag{2}$$

and $\eta = f - (\partial U_g/\partial y)_p$, $\mathrm{Ri} = N_v^2/(\partial U_g/\partial z)^2$, and $N_v^2 = g\partial \ln\theta_v/\partial z$, where g is gravity and $\theta_v = \theta(1 + 0.61q_v)$ is the virtual potential temperature, with θ the potential temperature and q_v the water vapor mixing ratio. As the symmetric stability is reduced, the tilt of the isentropes increases, and the convection can generate a stronger circulation because the compensating subsidence does proportionately less work against the ambient environment (Emanuel 1980). According to the theory, eventually a critical value is reached where the amount of work done against the environment becomes less than the amount of kinetic energy generated in the (convectively unstable) updraft. Under these conditions, the mesoscale circulation *enhances* the original convection. Using a linearized circulation integral, Emanuel (1980) finds this positive feedback effect can occur in (weakly) convectively unstable atmospheres for ambient symmetric stability parameter $S \approx 60$, a value quite common in the middle latitudes.

The present work extends the conditional symmetric instability theory to the nonlinear nonhydrostatic case with CAPE. This is done in two stages. First, the Lagrangian parcel model of Emanuel (1983a) is extended to the convectively unstable case. This analytical theory is then used to interpret the results from a nonlinear nonhydrostatic numerical mesoscale/cloud model. A rotating baroclinic (BCF) numerical simulation with CAPE is analyzed to assess the nonlinear effects of explicit convective momentum transport. Finally, a companion nonrotating barotropic (BTNF) simulation is performed to assess the overall effects of baroclinicity and rotation on the developing mesoscale circulation. No CSI is possible in the BTNF case. The initial conditions for the simulations are patterned after those observed over Louisiana in a recent case study (Jascourt et al. 1988), in which it was concluded that a mesoscale instability helped organize the convection on mesoscale time scales. The difference between the BCF and BTNF initial atmospheres is that the BCF vertical wind shear is baroclinic (in thermal wind balance, using $f = 7.292 \times 10^{-5}\ \mathrm{s}^{-1}$), while the BTNF shear is barotropic (no baroclinicity, $f = 0$).

The analytical theory shows that the addition of CAPE in the Lagrangian parcel model results in more vertical updrafts (still slanted up over the cool air) and larger growth rates than without CAPE. As in the moist-adiabatic case (Emanuel 1983a), the present model predicts that the baroclinically cool-side circulation will dominate.

The BCF simulation generally confirmed the parcel model predictions. Overall, the baroclinically cool-side circulation developed more rapidly, but with updrafts somewhat shallower than predicted by the parcel model. An equivalent of the analytical CSI sloping convective updraft/cool side outflow was found within the nonlinear numerical simulation. Large positive vertical heat fluxes within the convection were central to the development of this nonlinear CSI in that they enabled upward momentum transport across the isentropic surfaces. The convective momentum transport resulted in the formation of a subgeostrophic zonal momentum anomaly aloft, which then, through an imbalance in the pressure gradient and Coriolis forces, accelerated the meridional flow toward the baroclinically cool side. This meridional CSI outflow was found to be modulated by geostrophic adjustment, which tended to balance the convectively generated subgeostrophic zonal wind anomalies.

Interesting feedback effects were also observed in the BCF simulation. Mesoscale mass transports associated with the meridional CSI outflows ventilated the upper levels of the system, assisting in the development

of convection in the core and on the leading edge of the MCS on mesoscale time scales. The developing mesoscale circulation provided a favorable environment for these developments through moisture convergence into the core of the system at low levels. The mesoscale circulation itself developed in response to the convectively generated thermal wind imbalances, in an attempt to bring the system back into thermal wind balance. All of these processes helped the rotating baroclinic system grow upscale into a multicell structure resembling a squall line–type mesoscale convective system (MCS) (Houze et al. 1989), with a near-exponential increase in the circulation strength over the last 5 h of the simulation.

Comparison of the rotating baroclinic simulation to the companion nonrotating barotropic simulation showed that, overall, baroclinicity enhanced the growth of the simulated mesoscale convective system. This result supports the theoretical prediction of Emanuel (1980). The baroclinic system also produced more precipitation.

Based on the analysis of the present simulations and previous work, a new definition for slantwise convection is proposed: the term "slantwise convection" would refer to the combined convective updraft/cool side outflow that develops with the release of CSI in a convectively unstable atmosphere. Now, slantwise convection is often used to describe the sloping updrafts that result from CSI, without a distinction of whether CAPE is present. With CAPE, slantwise convection is associated with large vertical heat fluxes. This contrasts with classic CSI, which contains no CAPE and has negligible vertical heat fluxes. Although ordinary upright convection also has large vertical heat fluxes, by definition it does not occur in a rotating baroclinic environment and so does not develop the sloping updraft characteristic of CSI.

The numerical experiment design and methodology are described in section 2, followed by the simulation results in section 3. A summary and conclusions are presented in section 4.

2. Experiment design

A primary goal of the present study is to investigate the role of explicit convective momentum transport in nonlinear nonhydrostatic CSI in a convectively unstable baroclinic atmosphere. The basic tool for this investigation is a two-dimensional nonlinear numerical mesoscale/cloud model that resolves both the cloud and mesoscale space and time scales relevant for describing the phenomenon. The numerical model and initial atmosphere specification for this problem are described in the following subsections. As part of the analysis, a Lagrangian parcel model of CSI with CAPE is also developed. The parcel model and numerical model results are presented in section 3.

a. Numerical model

The numerical model is derived from a nonhydrostatic quasi-compressible set of equations (Anderson et al. 1985; Droegemeier and Wilhelmson 1987); convective clouds are predicted explicitly and an option exists for including the effects of baroclinicity and rotation on the convection. The dependent variables are the three wind components (u, v, w) in (x, y, z) coordinates, pressure (p), potential temperature (θ), water vapor (q_v), cloud water (q_c), and rainwater (q_r). The model is discretized for integration on an Arakawa C grid, using the finite-difference scheme of Droegemeier and Wilhelmson (1987) (see also Lilly 1965). Using the compact finite-difference notation:

$$\delta_{n\xi}\phi(\xi) = \frac{\phi(\xi + n\Delta\xi/2) - \phi(\xi - n\Delta\xi/2)}{n\Delta\xi} \quad (3)$$

$$\overline{\phi(\xi)}^{n\xi} = \frac{\phi(\xi + n\Delta\xi/2) + \phi(\xi - n\Delta\xi/2)}{2} \quad (4)$$

in which ϕ is any dependent variable, ξ is any independent coordinate, and $n\Delta\xi$ is the interval over which the operation takes place. The model is represented in numerical form as

$$\delta_{2t}u' = -\frac{1}{\bar{\rho}}\delta_y(\bar{\bar{\rho}}^y v\bar{u}^y) - \frac{1}{\bar{\rho}}\delta_z(\bar{\bar{\rho}}^z w\bar{u}^z) + f\bar{v}^y + D_u \quad (5)$$

$$\delta_{2t}v' = -\frac{1}{\bar{\bar{\rho}}^y}\delta_y(\overline{\bar{\bar{\rho}}^y v\,\bar{v}^y}^y) - \frac{1}{\bar{\bar{\rho}}^y}\delta_z(\overline{\bar{\bar{\rho}}^z w\,\bar{v}^z}^y) - f\overline{u'}^y - \frac{1}{\bar{\bar{\rho}}^y}\delta_y p' - \left(\frac{\overline{\theta'}^y}{\bar{\bar{\theta}}^y} + 0.61\overline{q_v'}^y - \frac{\overline{p'}^y}{\gamma\bar{\bar{p}}^y} - \overline{q_c'}^y - \overline{q_r'}^y\right) \times \frac{1}{\bar{\bar{\rho}}^y}\delta_y\bar{p} + D_v \quad (6)$$

$$\delta_{2t}w' = -\frac{1}{\bar{\bar{\rho}}^z}\delta_y(\overline{\bar{\bar{\rho}}^y v\,\bar{w}^y}^z) - \frac{1}{\bar{\bar{\rho}}^z}\delta_z(\overline{\bar{\bar{\rho}}^z w\,\bar{w}^z}^z) - \frac{1}{\bar{\bar{\rho}}^z}\delta_z p' + g\left(\frac{\overline{\theta'}^z}{\bar{\bar{\theta}}^z} + 0.61\overline{q_v'}^z - \frac{\overline{p'}^z}{\gamma\bar{\bar{p}}^z} - \overline{q_c'}^z - \overline{q_r'}^z\right) + D_w \quad (7)$$

$$\delta_{2t}p' = -\frac{\bar{C}_s^2}{\bar{\theta}_v}(\delta_y(\bar{\bar{\rho}}^y\bar{\bar{\theta}}_v^y v) + \delta_z(\bar{\bar{\rho}}^z\bar{\bar{\theta}}_v^z w)) \quad (8)$$

$$\delta_{2t}\theta' = -\frac{1}{\bar{\rho}}\overline{\bar{\rho}^y v\delta_y\theta}^y - \frac{1}{\bar{\rho}}\overline{\bar{\rho}^z w\delta_z\theta}^z + M_\theta + D_\theta \quad (9)$$

$$\delta_{2t}q_v' = -\frac{1}{\bar{\rho}}\overline{\bar{\rho}^y v\delta_y q_v}^y - \frac{1}{\bar{\rho}}\overline{\bar{\rho}^z w\delta_z q_v}^z + M_{qv} + D_{qv} \quad (10)$$

$$\delta_{2t}q_c' = -\frac{1}{\bar{\rho}}\overline{\overline{\rho}^{y} v\delta_y q_c'}^{y} - \frac{1}{\bar{\rho}}\overline{\overline{\rho}^{z} w\delta_z q_c'}^{z} + M_{qc} + D_{qc} \tag{11}$$

$$\delta_{2t}q_r' = -\frac{1}{\bar{\rho}}\overline{\overline{\rho}^{y} v\delta_y q_r'}^{y} - \frac{1}{\bar{\rho}}\overline{\overline{\rho}^{z} w\delta_z q_r'}^{z} + M_{qr} + D_{qr}, \tag{12}$$

where the $D_\varphi(M_\varphi)$ terms represent a turbulence (microphysics) parameterization.

The dependent variables are rewritten in terms of base state and perturbation parts such that any variable φ is represented as $\varphi = \bar{\varphi}(y, z) + \varphi'(y, z, t)$ in the two-dimensional framework. Quantities with overbars refer to the (hydrostatic and geostrophic) base-state environment, while primed variables are the predicted perturbations about this environment. Since $\bar{v} = \bar{w} = 0$ in the base state used in this study, $v = v'$ and $w = w'$ in the above equations. Also note the pressure forcing terms in (6) and (7) have been linearized about the geostrophic and hydrostatic base state, respectively (the base state is described in the following subsection). The quasi-compressible approximation here involves setting the sound speed C_s to a constant 100 m s^{-1} in (8), which is large enough so the sound waves do not strongly affect the gravity waves (Anderson et al. 1985). Neglect of the diabatic forcing term in (8) follows the convention of Klemp and Wilhelmson (1978).

The subgrid-scale mixing (D_φ) is parameterized using K theory, in which the diffusion coefficients are functions of the local environmental stability (Hill 1974). The diffusion terms in Eqs. (5)–(12) are represented by

$$D_\varphi = \frac{1}{\bar{\rho}}\left(\frac{\partial}{\partial y}\left(\bar{\rho}K\frac{\partial\varphi}{\partial y}\right) + \frac{\partial}{\partial z}\left(\bar{\rho}K\frac{\partial\varphi}{\partial z}\right)\right), \tag{13}$$

where φ can be any variable and $K = K_M$ for $\varphi = u, v$, or w, and $K = K_H$ when φ is any of the thermodynamic variables. (There is no diffusion of pressure and all φ variables are total quantities.) For this study, there is equal diffusion of heat and momentum (Pr $= K_H/K_M = 1$), where $K_M = \kappa l^2 t_t^{-1}$. Here κ is a viscosity coefficient [$\kappa = 0.4$; Hill (1974)], $l^2 = \Delta y \Delta z$ is a length scale of the largest unresolved eddies (Δy, Δz are grid spacings in the horizontal and vertical, respectively), and $t_t^{-1} = t_s^{-1} + t_b^{-1}$ is an inverse time scale for decay of the subgrid-scale turbulence. The total inverse time scale t_t^{-1} is composed of velocity deformation (t_s^{-1}) and buoyancy (t_b^{-1}) terms, which contribute equally to the diffusion (Hill 1974). The deformation-induced turbulence is activated when the Richardson number (Ri) falls below 0.25; buoyancy-induced turbulence occurs when the local lapse rate is superadiabatic (in unsaturated conditions, with respect to the dry adiabat; in regions of saturation, with respect to the moist adiabat). Following Klemp and Wilhelmson (1978), the mixing terms normal to the boundaries are neglected (e.g.,

$$\frac{1}{\bar{\rho}}\frac{\partial}{\partial z}\left(\bar{\rho}K\frac{\partial\varphi}{\partial z}\right) = 0$$

along the top and bottom boundaries, with a similar convention along the lateral boundaries).

The effect of surface friction on the interior flow is parameterized using the surface drag law formulation given in Wilhelmson and Chen (1982). Drag is a function of the horizontal perturbation kinetic energy and is applied to the perturbation u' and v' variables at the first level above ground only. The frictional drag coefficient C_D is set to a constant 0.002. No heat flux or evaporation of water from the surface exists in the current version of the model.

The microphysics treatment is the water-only version of Lin et al. (1983). The microphysics parameter definitions (M_φ) and conversion rates are given in appendix A, while further details can be found in Lin et al. (1983).

The boundary conditions follow the convention of Klemp and Wilhelmson (1978). Along the bottom and top of the domain, $w = 0$. The top condition reflects upward propagating gravity waves impinging on the model top back down into the domain (which is nonphysical). This problem is reduced by placing a Rayleigh friction zone (sponge) (Clark 1977) near the top (uppermost ten grid points) to damp out the gravity waves, using coefficients given by Durran and Klemp (1983). Reflections of gravity waves off the lateral boundaries are reduced by applying the radiation condition of Klemp and Wilhelmson (1978) at the sidewalls, which allows outward propagating gravity waves to exit the domain.

Two numerical filters are applied to the predicted variables during the integration. Although the cascade of energy into the $2\Delta y$ to $4\Delta y$ scale, for example, is largely eliminated by the advection scheme, a weak fourth-order horizontal numerical filter (second order next to the lateral boundaries) is applied to remove any noise that might find its way to those scales (Klemp and Wilhelmson 1978). Time filtering is also required because the leapfrog time scheme is numerically unstable without it. An Asselin (1972) time filter first proposed by Robert (1966) is also applied to the model variables as the model is integrated.

b. Initial atmospheres

Two two-dimensional (y, z) initial atmospheres were required for the two numerical simulations: one is baroclinic (for the BCF simulation), the other is barotropic (for the BTNF simulation). The two atmospheres contain the same domain center sounding and zonal wind $U(z)$ profiles. They differ in that the (initial) BCF shear is in thermal wind balance, while the

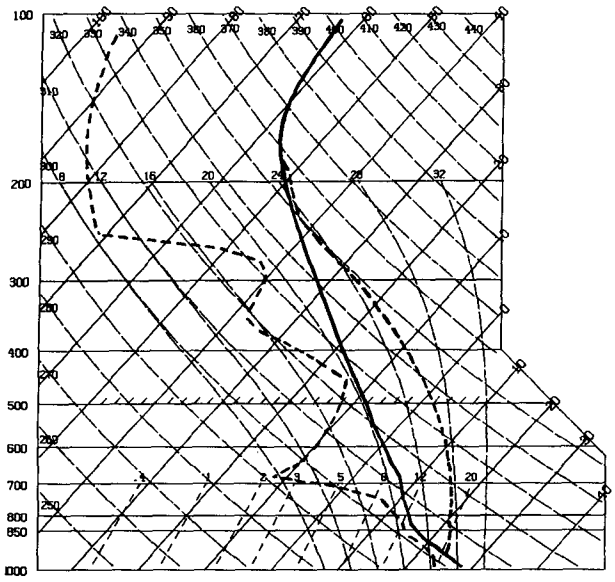

FIG. 1. Skew$T$–log$p$ center-column thermodynamic sounding: temperature (solid), dewpoint temperature (dashed). The sounding contains a CAPE (SCAPE) of 2400 (2600) J kg^{-1}. The maximum temperature profile produced within the cloud is also shown as a dashed line to the right of the environmental temperature profile.

BTNF shear is not (atmosphere is horizontally homogeneous). The details are described below.

The baroclinic atmosphere generated for this study is an idealization of the precedent environment from a case study in which weak ambient symmetric stability was hypothesized to be important to the observed convective organization on mesoscale time scales (Jascourt et al. 1988). The most important atmospheric features from that case study were

1) high CAPE over the entire Louisiana region with deep low-level moisture [relative humidity (RH) $>$ 85% to 700 mb] and no capping inversion,
2) nearly unidirectional mean vertical wind shear (zonal shear of 20 m s^{-1} per 10 km),
3) relatively weak symmetric stability ($S \approx 30$, stratified in layers) in the midtroposphere as diagnosed by a north–south 12 UTC cross section through the area, and
4) little external dynamical forcing over the area (vorticity advections, frontogenesis, etc.).

Guided by the above observations and previous work in CSI theory, the baroclinic atmosphere was generated by specifying constant midtropospheric static stability and geostrophic wind shear so that the symmetric stability [Eq. (2)] was uniform across the domain ($S \approx 32.5$). This was accomplished by first generating the (hydrostatic) domain center sounding with the desired static stability profile (Fig. 1), and then using the specified wind field in the thermal wind equation to obtain the two-dimensional virtual temperature field, using $f = 7.292 \times 10^{-5}$ s^{-1} (appropriate for southern Louisiana at latitude $\phi = 30°$). The pressure field was obtained from the specified wind and virtual temperature fields using the geostrophic wind relation. After a final hydrostatic check, the potential temperatures and mixing ratios were retrieved from the virtual temperature, pressure, and specified humidity fields, using an iterative technique (Seman 1991). To minimize horizontal variations in CAPE, the relative humidity was specified to increase linearly from south to north in the boundary layer (below 1 km), using the specified domain center relative humidity as a starting point. Figure 2 shows the initial baroclinic base state.

The center sounding itself was constructed by blending the 1500 UTC surface observations over southern Louisiana with an idealized 1200 UTC 5 June 1986 sounding from LCH (Lake Charles, Louisiana); it contains constant static stability (N_v^2) above a mixed layer 1-km deep up to a stratosphere (starting at 15 km) with higher static stability. The zonal wind field $U_g(z)$ features a constant vertical wind shear of 20 m s^{-1}/10 km below the stratosphere, with reverse shear above to the top of the domain (there is no meridional wind in the base state).

Construction of the barotropic environment was much simpler. The domain center sounding and zonal wind field were specified as above, but since $f \equiv 0$, this atmosphere is horizontally homogeneous so that all horizontal locations have the same vertical sounding.

c. *Numerical simulations*

Two 8-h simulations are performed with the mesoscale/cloud model on a 600-km (horizontal) by 22-km (vertical) domain. The BCF simulation starts with the baroclinic atmosphere (where $f = 7.292 \times 10^{-5}$ s^{-1}), while the BTNF uses the barotropic initial atmosphere ($f = 0$). The grid resolution is 1 km (horizontal) by 400 m (vertical) with an imposed "pseudosound"

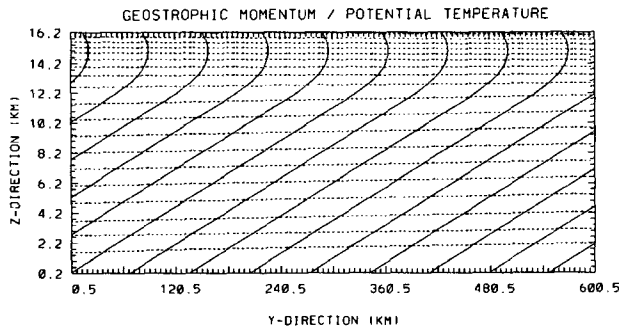

FIG. 2. Initial baroclinic base state showing geostrophic momentum ($M_g = U_g - fy$) and potential temperature (θ) surfaces. Contour interval is 10 m s^{-1} for M_g (solid) and 5 K for θ (dashed). M_g and θ both increase with height and decrease to the north ($+y$ direction). The state is symmetrically stable because the M_g surfaces are more vertical than the θ, and $\partial M_g/\partial y < 0$.

speed of 100 m s^{-1} in both simulations. A time step of 1 second is used to satisfy the CFL condition for linear stability ($\Delta t < 1.85$ s). A single warm moist bubble initiates the convection in the center of the domain [$\theta_{max} = 1.5$°C, identical to that used by Klemp and Wilhelmson (1978) except that it is centered at the first model level above ground]. The water vapor perturbations are specified so that the relative humidity inside the bubble is the same as that of ambient environment ($q_{vmax} = 1.72$ g kg^{-1}). Note that the (y, z) plane of simulation here is *perpendicular* to the ambient wind with the circulation axis of the modeled convection parallel to the mean wind; in many two-dimensional studies of deep, moist convection, the ambient wind blows *parallel* to the plane in which the convection is modeled (e.g., Moncrieff and Miller 1976; Thorpe et al. 1982; Rotunno et al. 1988; Fovell 1991).

d. Diagnostics averaging

Many of the diagnostic parameters shown have been time and/or space averaged. When a parameter is space averaged, centered horizontal averaging is used (Tripoli 1990, personal communication). For 10-km horizontal space averaging, (10 km/Δy) + 1 grid points enter into the sum. Away from the lateral boundaries at an interior point $\hat{j}$, the new value becomes

$$\phi^{new} = \frac{1}{N+1} \sum_{j=N/2}^{\hat{j}+N/2} \phi^{old},$$

where ϕ is any diagnostic parameter and $N = (10 \text{ km}/\Delta y)$. As one approaches the lateral boundaries, progressively fewer points are brought into the average until at the last interior point, $N = 3$. Time averaging is also employed to isolate a mesoscale time scale component of a diagnostic parameter. This is accomplished by taking a simple linear average of raw (or space averaged) data. Since the basic model fields were archived at 4-minute time intervals, a 1-h time-averaged field contains 15 individual fields.

3. Results

The results are presented in two subsections: in section 3a a Lagrangian parcel model with CAPE is developed, while in section 3b the two numerical simulations (BCF, BTNF) are examined. The numerical analysis focuses on the BCF simulation and in particular on the development of the circulation associated with the mesoscale convective system. Part of the analysis involves a comparison of the BCF system to the analytical theory and the BTNF simulation.

a. Two-dimensional Lagrangian parcel model

The equations of motion for the conditional symmetric instability problem under moist adiabatic conditions ($N^2 = 0$) were derived by Emanuel (1983a). Following his work, those equations are extended to the case in which CAPE is present ($N^2 < 0$). For two-dimensional inviscid motions in the (y, z) plane

$$\frac{dv}{dt} = \frac{d^2y}{dt^2} = f(\bar{U}_z z - \bar{\eta} y) \tag{14}$$

$$\frac{dw}{dt} = \frac{d^2z}{dt^2} = -N^2 z + f\bar{U}_z y, \tag{15}$$

where $\bar{U}_z$ is the vertical wind shear of the base-state zonal wind (in thermal wind balance with a meridional temperature gradient), $\bar{\eta}$ is the absolute vorticity ($f - \partial\bar{U}/\partial y$), and N^2 is a measure of the static stability under saturated conditions. Here a constant $N^2 = (g/\theta_0)\partial\theta_w/\partial z$ is assumed (Xu 1986), where θ_0 is a reference potential temperature and θ_w is the wet-bulb potential temperature. Figure 3 shows schematically the relative orientation of base-state absolute momentum ($\bar{M} = \bar{U} - fy$) and buoyancy surfaces for this problem. The base state differs from that studied by Emanuel only in that the atmosphere contains CAPE, and so the buoyancy surface B is bent back to signify that the vertical lapse rate is greater than moist adiabatic.

Noting that $\bar{\eta} \ll \bar{U}_z$, the $\bar{\eta}$ term in (14) is neglected (Emanuel 1983a). This allows for direct comparison to Emanuel's results and simplifies the solution of the current problem considerably, without changing the essential dynamics under study. Differentiating (15) twice in time and substituting from (14) yields

$$\frac{d^4z}{dt^4} + N^2\frac{d^2z}{dt^2} - f^2\bar{U}_z^2 z = 0. \tag{16}$$

Solutions to (16) have the form $z \sim \exp(\sigma t)$, or

$$\sigma^4 + N^2\sigma^2 - f^2\bar{U}_z^2 = 0, \tag{17}$$

from which

$$\sigma^2 = -\tilde{N}^2 \pm \sqrt{\tilde{N}^4 + \tilde{U}^4}, \tag{18}$$

where $\tilde{N}^2 = N^2/2$ and $\tilde{U}^2 = f\bar{U}_z$. The positive (nega-

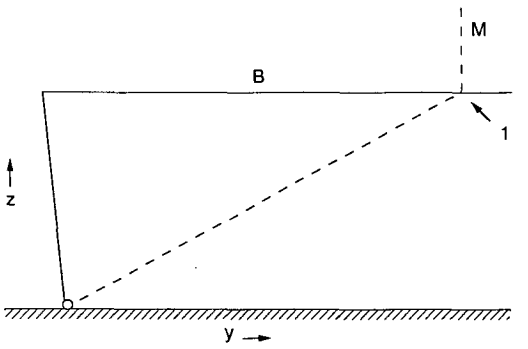

FIG. 3. Relative orientation of M (dashed) and B (solid) surfaces for the simple nonhydrostatic conditional symmetric instability problem with CAPE. The stable equilibrium position of the surface tube is at point 1.

tive) root in (18) corresponds to growth (oscillations) of disturbances. Also note that for $N^2 = 0$, the eigenvalues $\sigma^2 = \pm f\bar{U}_z$ from Emanuel's (1983a) analysis are recovered. The growth rates with CAPE ($N^2 < 0$) are larger than those for moist-adiabatic conditions ($N^2 = 0$). The growth rate ratio

$$\lambda = \frac{\sigma_{\text{CAPE}}}{\sigma_{\text{NO CAPE}}} = \left(\frac{-\tilde{N}^2 + \sqrt{\tilde{N}^4 + \tilde{U}^4}}{\tilde{U}^2}\right)^{1/2} \quad (19)$$

shows that (for $\tilde{U}^2 = 1.5 \times 10^{-7}\ \text{s}^{-2}$ in this study) λ ranges from about 2.5 for $N^2 = -1 \times 10^{-6}\ \text{s}^{-2}$ (N^2 value used by Xu (1986), with small CAPE $= -N^2H^2/2 \approx 50\ \text{J kg}^{-1}$ for $H = 10$ km), to 18.5 for $N^2 = -5 \times 10^{-5}\ \text{s}^{-2}$ (appropriate for this study with large CAPE $\approx 2500\ \text{J kg}^{-1}$).

The general solution of (14)–(15) with arbitrary initial conditions is

$$y = \frac{1}{\tilde{U}^2}\left[\left(\frac{w_0}{\sigma_1} + \frac{\tilde{U}^2 v_0 - (\sigma_1^2 + N^2)w_0}{\sigma_1(\sigma_1^2 + \sigma_2^2)}\right)(\sigma_1^2 + N^2) \times \sinh(\sigma_1 t) + \left(\frac{\tilde{U}^2 v_0 - (\sigma_1^2 + N^2)w_0}{\sigma_2(\sigma_1^2 + \sigma_2^2)}\right) \times (\sigma_2^2 - N^2)\sin(\sigma_2 t)\right] \quad (20)$$

$$z = \left(\frac{w_0}{\sigma_1} + \frac{\tilde{U}^2 v_0 - (\sigma_1^2 + N^2)w_0}{\sigma_1(\sigma_1^2 + \sigma_2^2)}\right)\sinh(\sigma_1 t) - \left(\frac{\tilde{U}^2 v_0 - (\sigma_1^2 + N^2)w_0}{\sigma_2(\sigma_1^2 + \sigma_2^2)}\right)\sin(\sigma_2 t), \quad (21)$$

where the initial velocity of the tube is (v_0, w_0), starting at $y = z = 0$, with $\sigma_1 = (-\tilde{N}^2 + \sqrt{\tilde{N}^4 + \tilde{U}^4})^{1/2}$ and $\sigma_2 = (\tilde{N}^2 + \sqrt{\tilde{N}^4 + \tilde{U}^4})^{1/2}$. The $\sin(\sigma_2 t)$ terms in the above equations give rise to oscillations in the solution about the path $v_0 = w_0(\sigma_1^2 + N^2)/\tilde{U}^2$. For the special case in which $v_0 = w_0(\sigma_1^2 + N^2)/\tilde{U}^2$ (or at large time),

$$y = \left(\frac{w_0}{\sigma_1}\right)\left(\frac{\sigma_1^2 + N^2}{\tilde{U}^2}\right)\sinh(\sigma_1 t) \quad (22)$$

$$z = \left(\frac{w_0}{\sigma_1}\right)\sinh(\sigma_1 t). \quad (23)$$

In this case, the meridional displacement is scaled by the factor $(\sigma_1^2 + N^2)/\tilde{U}^2$ relative to the vertical displacement. For $N^2 = -5 \times 10^{-5}\ \text{s}^{-2}$ ($N^2 = -1 \times 10^{-6}\ \text{s}^{-2}$, Xu 1986), $(\sigma_1^2 + N^2)/\tilde{U}^2$ is 0.003 (0.15) for $\tilde{U}^2 = 1.5 \times 10^{-7}\ \text{s}^{-2}$. Thus, for a vertical displacement to $z = H$, the meridional displacement is $0.003H$ ($0.15H$), with an angle of ascent of about 89.8° (81.5°) as measured from the horizontal. Also, for $N^2 = 0$, Emanuel's (1983a) solution is recovered, in which case the angle of ascent is 45°.

The general expressions for the meridional and vertical velocity of the tube are

$$v = \frac{1}{\tilde{U}^2}\left[\left(\frac{\tilde{U}^2 v_0 + (\sigma_2^2 - N^2)w_0}{(\sigma_1^2 + \sigma_2^2)}\right)(\sigma_1^2 + N^2) \times \cosh(\sigma_1 t) + \left(\frac{\tilde{U}^2 v_0 - (\sigma_1^2 + N^2)w_0}{(\sigma_1^2 + \sigma_2^2)}\right) \times (\sigma_2^2 - N^2)\cos(\sigma_2 t)\right] \quad (24)$$

$$w = \left(\frac{\tilde{U}^2 v_0 + (\sigma_2^2 - N^2)w_0}{(\sigma_1^2 + \sigma_2^2)}\right)\cosh(\sigma_1 t) - \left(\frac{\tilde{U}^2 v_0 - (\sigma_1^2 + N^2)w_0}{(\sigma_1^2 + \sigma_2^2)}\right)\cos(\sigma_2 t). \quad (25)$$

For the limit of small (v_0, w_0) and large time, the oscillation effect may be ignored, and using (22)–(23) and the definition of sinh( ), one obtains

$$y = \left(\frac{\sigma_1^2 + N^2}{\tilde{U}^2}\right)z, \quad w = \sigma_1 z, \quad v = \left(\frac{\sigma_1^2 + N^2}{\tilde{U}^2}\right)\sigma_1 z. \quad (26)$$

For small CAPE ($N^2 = -1 \times 10^{-6}\ \text{s}^{-2}$), with $\tilde{U}^2 = 1.5 \times 10^{-7}\ \text{s}^{-2}$ and the definition of σ_1 given above, the vertical (meridional) velocity of the tube approaches 10 (1.5) m s^{-1} at $z = H$, where H is taken as 10 km. For large CAPE ($N^2 = -5 \times 10^{-5}\ \text{s}^{-2}$) and $\tilde{U}^2 = 1.5 \times 10^{-7}\ \text{s}^{-2}$, the vertical (meridional) velocity of the tube approaches 71 (0.2) m s^{-1} at $z = H$. The vertical velocity should be thought of as an upper limit in the absence of adverse perturbation pressure gradients, turbulence, and water loading, which would be generated by the convection in reality. As stated by Emanuel (1983a), neglect of turbulent mixing is a weakness of the parcel model. Overall, it provides a useful upper bound for the updraft strength and tilt for deep, moist convection in a rotating baroclinic environment, and predicts that the baroclinically cool-side circulation will dominate.

After the tube reaches $z = H$, $y = [(\sigma_1^2 + N^2)/\tilde{U}^2]H$, it will begin accelerating northward toward its equilibrium point (Fig. 3) while also executing a vertical oscillation about the buoyancy surface B at $z = H$. Following Emanuel (1983a), the vertical oscillation is ignored and (14) is solved for the horizontal path of the tube. The initial conditions for this part of the integration are taken to be

$$y_0 = \left(\frac{\sigma_1^2 + N^2}{\tilde{U}^2}\right)H, \quad v_0 = \left(\frac{\sigma_1^2 + N^2}{\tilde{U}^2}\right)\sigma_1 H$$

and the vertical velocity is assumed to vanish. The solution to (14) with these initial conditions is

$$y = \left(\frac{\sigma_1^2 + N^2}{f\bar{U}_z} - \frac{\bar{U}_z}{f}\right) H\cos(ft) + \frac{\bar{U}_z H}{f}. \quad (27)$$

The maximum meridional velocity of the tube is $v_{max} \approx \bar{U}_z H$, which occurs at $y = \bar{U}_z H/f$, while the maximum penetration of the tube is at $y_{max} = 2\bar{U}_z H/f$. The parcel model predicts that by time $t = \pi/2f$ (6 h) the tube will acquire a maximum velocity comparable to the ambient flow at $z = H$, at a horizontal distance of approximately $27H$ (270 km) from the initial updraft.

b. *Numerical simulations*

This subsection contains three parts focusing on various aspects of the the BCF simulation. The first part gives an overview of the BCF simulation in general terms, including a comparison of BCF and BTNF mesoscale circulation characteristics. The second part discusses the role of zonal momentum anomalies in the numerically simulated nonlinear CSI. The third part presents diagnostics showing the roles of convective momentum transport and nonlinear CSI in the growth of the BCF mesoscale circulation.

1) General characteristics

As described in section 2, a single warm moist bubble initiates the convection in the center of the domain. This convection transports significant amounts of low-level zonal momentum upward, disrupting the thermal wind balance and resulting in the formation of a subgeostrophic momentum anomaly at upper levels (Fig. 4), as described by Newton (1950). This unbalanced momentum anomaly is very important in the nonlinear evolution of the BCF system in that it fosters the development of the simulated CSI and associated mesoscale circulation. Note that the net effect of the convection on the potential temperature field is relatively small, even though the vertical fluxes of mass and heat are also large.

Physically, a net upward vertical momentum transport occurs as latent heating within the updraft allows the low-level momentum to be carried upward across isentropic surfaces (Fig. 4). Assuming two-dimensional ($\partial/\partial x = 0$), frictionless conditions, the zonal momentum equation can be written as

$$\frac{dM}{dt} = 0, \quad (28)$$

where $M = U - fy$, showing that M is conserved following the motion. On the other hand, the potential temperature equation

$$\frac{d\theta}{dt} = M_\theta \quad (29)$$

shows that entropy increases when there is a net latent heating, where M_θ represents the net effect of sources and sinks of θ due to microphysical processes within the cloud. Because the ambient potential temperature increases with height, the condensational source of θ in the updraft means the surfaces of constant M must move *upward* relative to the surfaces of constant θ. Viewed in another way, the vertical heat flux in the convection enables the momentum surfaces to be drawn upward to higher values of potential temperature. That is, the air within the updraft rises moist adiabatically to its level of neutral buoyancy, carrying momentum from low levels with it. Without diabatic heating (or friction), the M and θ surfaces may be deformed (by propagating gravity waves, for example), but the area enclosed by two M and θ surfaces is conserved,

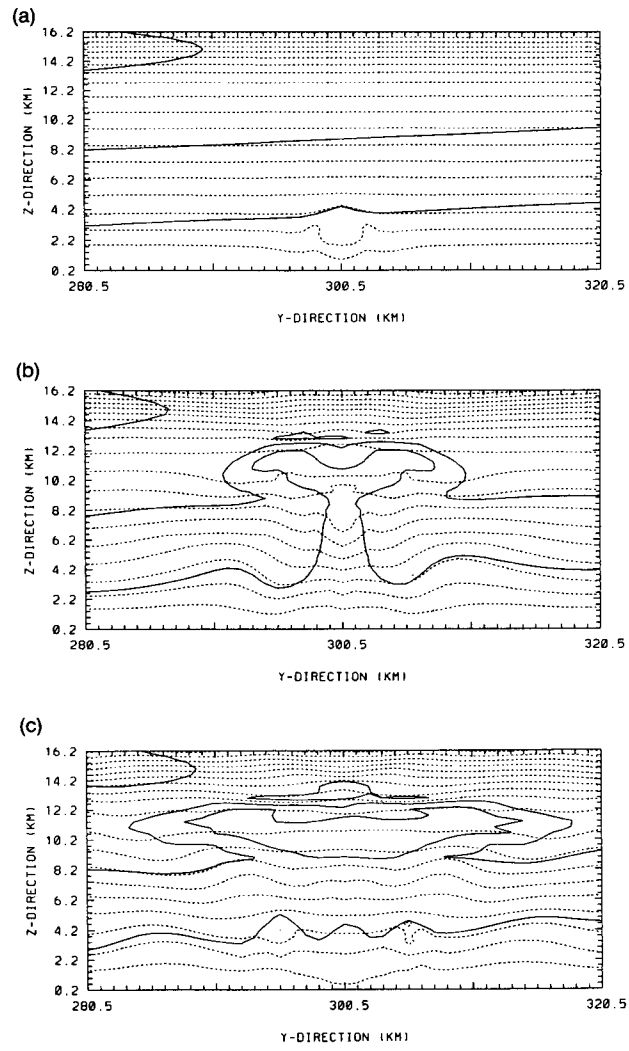

FIG. 4. Total momentum ($M = U - fy$) and potential temperature (θ) cross sections at (a) 20, (b) 40, and (c) 60 min for the rotating, baroclinic shear simulation (BCF). Contour interval is 10 m s^{-1} for M (solid) and 5 K for θ (dashed). Note the upward movement of the M surfaces relative to the θ, and the outward propagating gravity waves. Thermal wind balance is disrupted by the convection.

constrained by the conservation of dry potential vorticity.

Part of the buoyant energy generated in the updraft (vertical heat flux) is converted into a pair of deep internal gravity waves, which propagate away from their source (Fig. 4b,c), leaving a relatively small net effect on the cloud-scale mass and temperature fields. This occurs since the convection is small dynamically compared to Rossby radius of deformation. The horizontal (vertical) half-wavelength of the momentum anomaly is approximately 25 (4) km (Fig. 4c), which is small compared to the corresponding Rossby radius of deformation[1] ($L_R \approx 200$ km). On these small dynamical scales, convectively generated momentum anomalies are much more robust than mass or temperature anomalies (Matsumoto 1961; Emanuel 1980; Schubert et al. 1980; Barwell and Bromley 1988). This characteristic is important for the evolution of the system because it enables the outflow branch of the nonlinear CSI to develop.

The sequence of cross sections in Fig. 4 also shows that the momentum transport within the convection tilts the vortex tubes (M surfaces), resulting in anomalously high (low) values of absolute vorticity $\eta_\theta = -(\partial M/\partial y)_\theta$ along the southern (northern) flank of the original convection. The vorticity anomalies generated by the convection are one to two orders of magnitude larger than f in absolute value.

Following the initial convective plume, several more convective events occur over the 8-h BCF simulation. Figure 5 summarizes the convective activity in a time series of vertical (and meridional) wind maxima for the last 6 h of the simulation. [Because the initial convective cell is much stronger ($w_{max} = 35$ m s^{-1}) than the later convection, for reasons of visual clarity it is not shown in the series.] The horizontal locations of the vertical wind maxima (w_{max}) are not given, but they generally occur within 25 km of the original cell. As a measure of the baroclinically cool-side outflow, the meridional wind maxima (v_{max}) series focuses on the $y > 310$ km region, between 7 and 12 km elevation.

Several interesting features are apparent in the time series. First, the w_{max} series shows that four distinct convective developments occur between 2 and 8 h, quasi-periodic in time with about 90 min between peak updrafts. Overall, the convection is weaker than the initial cell, and there is a tendency for the later convection to be more mesoscale in character, with updrafts that are somewhat weaker but last longer. Note also a general upward trend in the minimum values in w_{max} between peak updrafts: from about 1 m s^{-1} at 4 h

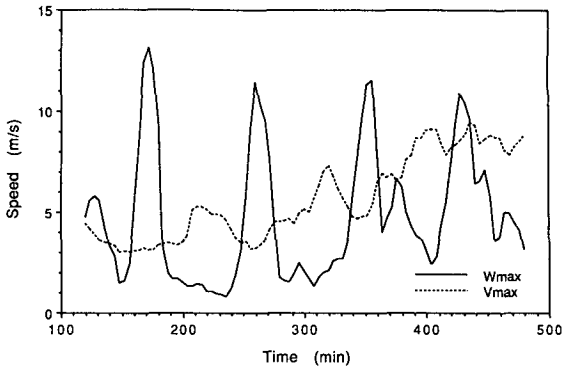

FIG. 5. Time series of vertical and baroclinically cool-side meridional velocity extremes for hours 2–8 (120 to 480 min) for the rotating baroclinic (BCF) simulation [W_{max} (solid) and V_{max} (dashed) in m s^{-1}].

to about 3 m s^{-1} at the end of the simulation. This occurs without a trend in the domain mean vertical motion, and represents a development of midlevel mesoscale updraft with the system. It is located near the center of the domain, at an elevation of between 4 and 7 km. [No growing mesoscale updraft was evident in the BTNF simulation, and in fact the convection weakened over the last 4 h of the simulation (figure not shown).]

The rather persistent convection in the BCF system transported significant amounts of zonal momentum vertically, and the upper-level negative momentum anomaly increased in size within the growing system (compare Figs. 4 and 6). A significant negative momentum anomaly also formed in the BTNF system (not shown); however without rotation, the zonal momentum field is essentially uncoupled from the rest of the system, aside from using it for the turbulence parameterization [see (5) and (6)]. More will be said about the BCF zonal momentum anomalies later.

The cool-side meridional wind maxima (v_{max}) time series also exhibits a general upward trend over the last 6 h of the simulation. The v_{max} increases from about 3 m s^{-1} at 2 h to more than 8 m s^{-1} by 8 h, with some variability on mesoscale time scales, and the maxima are generally located within 50 km downstream of the convection (not shown). Examination of individual meridional wind cross sections (archived at 4 minute intervals) revealed that the wind maxima are generally relatively small jetlike features typically 500–1000 m deep and roughly 5 km in length, and often propagate faster than the mean flow. This behavior may be related to nonlinearities in the outflow, but further analysis is beyond the scope of this paper.

Comparison of the numerical model w_{max} and v_{max} time series for the simulation with the Lagrangian parcel model reveals that the parcel model overestimates the maxima in w (35 m s^{-1}) and v (9 m s^{-1}) by a factor of ~2. Also, the location of the maximum meridional

[1] Following Schubert et al. (1980), the Rossby radius of deformation is defined here as $L_R = C_g/f$, where C_g is the gravity wave phase speed [$=N\delta Z/(2\pi)$, Klemp and Wilhelmson 1978]. For a mode with a vertical wavelength $\delta Z = 8$ km, $C_g \approx 14.5$ m s^{-1}, and $L_R \approx 200$ km.

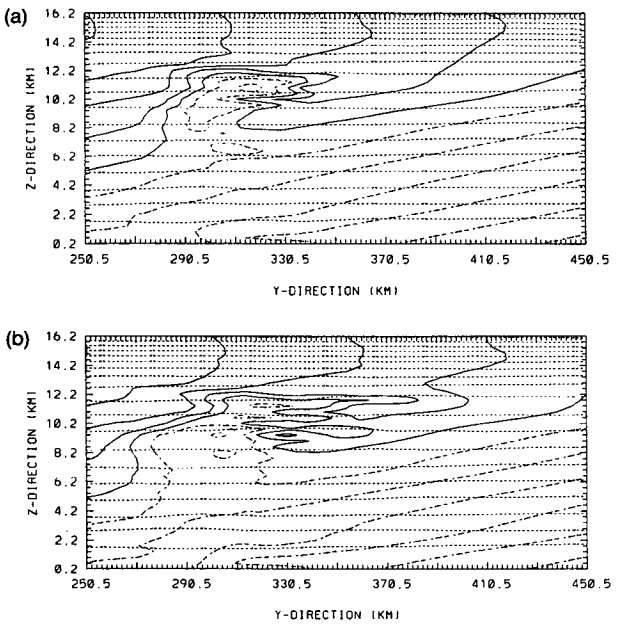

FIG. 6. Time-averaged total momentum/potential temperature (M, θ) cross sections for hours (a) 4–5 and (b) 7–8 for the rotating, baroclinic shear simulation (BCF). Horizontal space averaging of 20 km was applied to both fields. Momentum contours are solid (long dashes for negative values of M), with short dashes for potential temperature. Contour interval is 5 m s^{-1} (5 K) for M (θ), starting at 0 m s^{-1} (300 K).

velocities predicted by the parcel model is farther downstream (~270 km) than simulated by the numerical model (50 km). The strength and horizontal extent of the meridional outflow is regulated by geostrophic adjustment, which acts to balance the negative zonal wind anomaly (compare Figs. 6 and 7). The deep modes are most affected, while the shallow outflow modes are able to progress farther northward (Figs. 6a,b). It is interesting that there is strong horizontal mixing at the downstream edge of the anomaly, where the absolute vorticity is negative (Fig. 8). This mixing behavior is consistent with the SI theory of Houghton and Young (1970) and Stevens and Ciesielski (1986), who show that the shallow modes should grow the fastest.

Estimates of the w_{max} and v_{max} based on parcel energetics provide similar predictions for the simulated maxima. From the initial[2] SCAPE of 2600 J kg^{-1}, 200 J kg^{-1} of which is initially available for the quasi-horizontal meridional outflow, a maximum updraft (meridional outflow) of about 70 (20) m s^{-1} is predicted, which is also a factor of ~2 larger than simulated.

Multiple mesoscale updrafts developed during the last 3 h of the BCF simulation (Fig. 9). Examination of the 1-h time-averaged w' fields revealed that the updrafts generally tilted over the baroclinically cool air with angles somewhat greater than 70° above the horizontal, which is shallower than expected from the Lagrangian parcel model (89.8°). The parcel model cannot predict the development of multiple updrafts. Diagnostics to be presented in the next section show that meridional mass divergence tendencies associated with the nonlinear CSI outflows can help explain the development of the multiple updrafts.

The time-averaged BCF meridional wind fields for hours 4 to 8 revealed a vertically alternating (±) signature in the cool-side outflow. This horizontal mixing developed in the cool-side outflow anvil (Fig. 9) within regions of negative isentropic vorticity (Fig. 8). Occasionally, the horizontal mixing increased to the point that the Ri became subcritical (Ri < 0.25) and the turbulence parameterization was activated (figure not shown). There is evidence suggesting that this type of mixing occurs in nature as well. For example, Houze et al. (1989) show Doppler radar analyses of the 10–11 June 1985 PRE-STORM squall line that depict a region of turbulence (Ri < 0.25) within the back edge of the anvil. This corresponds to the baroclinically cool-side anvil in the BCF simulation. Overall, it appears that the mixing contributes to a breakup of the rather continuous negative vorticity anomaly generated by the initial convection (Fig. 8a) into smaller, weaker anomalies by the end of the simulation (Fig. 8c). This occurs as the entire region of negative vorticity is stretched out horizontally downstream by the developing circulation (Fig. 8a,b). The breakup of negative absolute vorticity by mixing was also seen in the simulations of dry, viscous nonlinear symmetric instability performed by Thorpe and Rotunno (1989). Note that while the negative vorticity has been largely eliminated

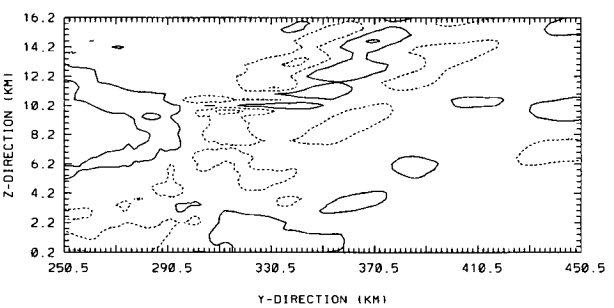

FIG. 7. Time-averaged ageostrophic zonal wind for hours 4–6 for the BCF simulation. Horizontal space averaging of 20 km was applied to the raw values. Contour interval is 4 m s^{-1}, starting at −6 m s^{-1}. Minimum value: −8.15 m s^{-1}; maximum: 6.53 m s^{-1}.

[2] In a baroclinic atmosphere with no horizontal wind shear, Emanuel (1983b) shows the slantwise convective available potential energy (SCAPE) can be evaluated as the sum of the potential energy due to ordinary upright convection (CAPE) and that resulting from centrifugal forces (conservation of angular momentum of the parcel): SCAPE = CAPE + $\frac{1}{2}(\Delta U)^2$, where ΔU is the vertical (geostrophic) wind shear over the depth of the convection.

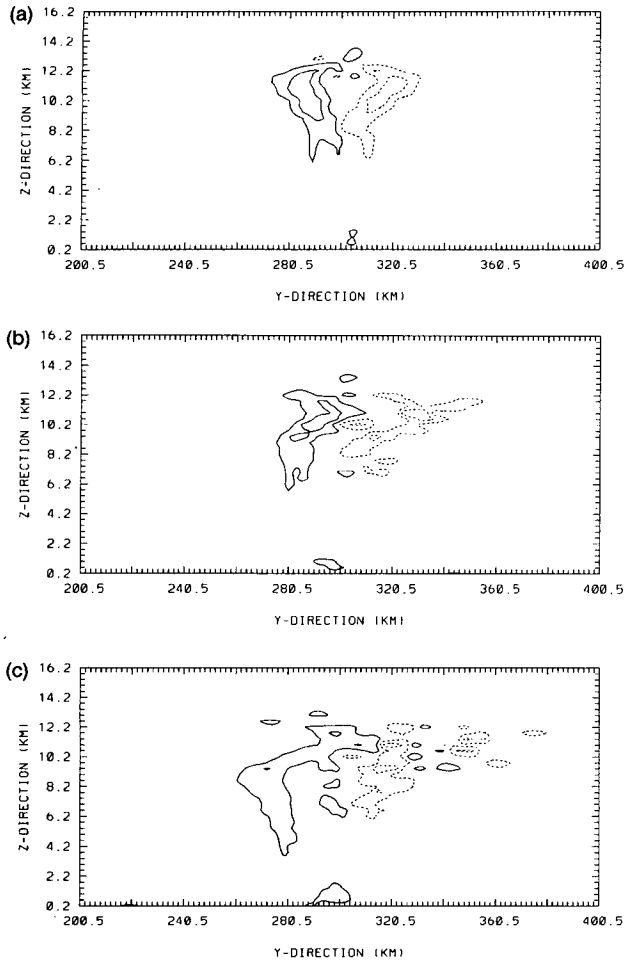

FIG. 8. Time-averaged isentropic absolute vorticity for hours (a) 1–2, (b) 4–5, and (c) 7–8 for the rotating, baroclinic shear simulation (BCF). Horizontal space averaging of 10 km was applied to the vorticity values. Contour interval is 4×10^{-4} s^{-1}, with -6×10^{-4} s^{-1} the minimum contour (dashed).

in the downstream outflow, a deep negative anomaly has redeveloped back closer to the core of the system (Fig. 8c). This anomaly has been generated by vertical momentum transport in the deep convection there, and is somewhat weaker than the original negative anomaly (Fig. 8a). It is interesting to note that rather large (and persistent) negative absolute vorticity anomalies have been observed in the cool-side outflows of real mesoscale convective complexes (Maddox 1983).

As hypothesized by Emanuel (1983a), a baroclinically cool-side mesoscale circulation dominates as the BCF system matures (Figs. 10, 12). The circulation is characterized by a nearly vertical updraft branch, quasi-horizontal outflow, and a more gentle subsidence branch oriented approximately along the ambient M surfaces (see also Figs. 2, 6). The circulation strength increases nearly exponentially over the last 5 h of the simulation (Fig. 12), suggesting a mesoscale instability effect within the simulation.

Note also that the circulation associated with the BCF system is less transient than that of the BTNF system (compare Figs. 10 and 11). Although the BTNF circulation maxima briefly attains the strength of that in the BCF system, it experiences a rapid breakdown in the last 2 h while the BCF continues to grow. In essence, the circulation associated with the BTNF convection expands outward (Fig. 11) to a physical scale consistent with the infinite Rossby radius of deformation for its environment. The expansion beyond the simulation boundaries could partly explain the decay in circulation growth (Fig. 12). (Whether its circulation would remain more coherent on a larger domain is not clear; however, some recent simulation results

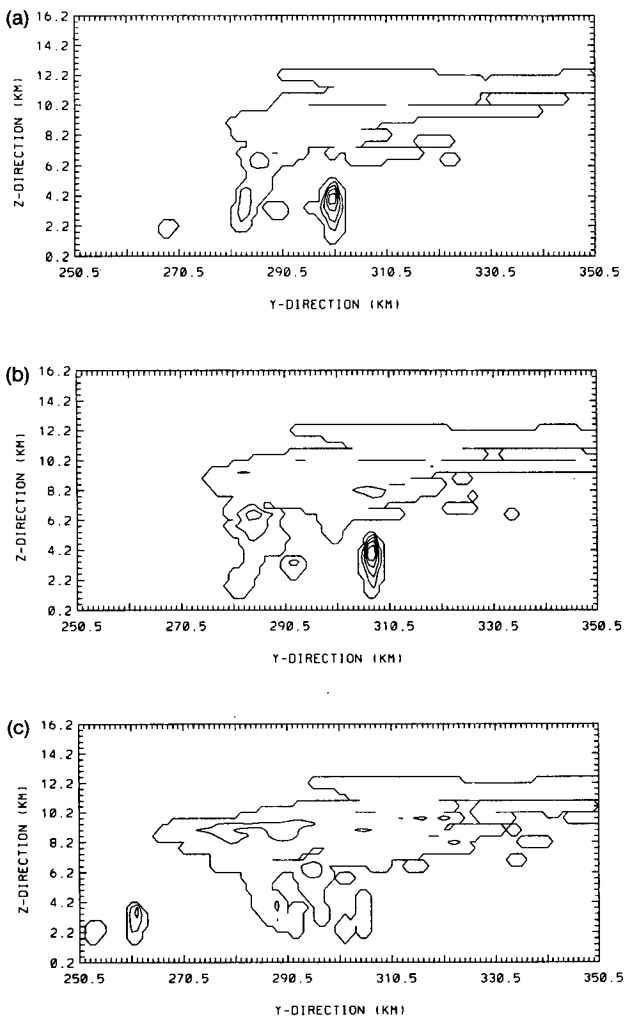

FIG. 9. Cloudwater at (a) 344, (b) 424, and (c) 480 min for the rotating baroclinic simulation (BCF). Contour interval is 1 g kg^{-1}, starting at 0 g kg^{-1}. Multiple mesoscale updrafts develop, and evaporation of the cloud anvil is apparent near $y = 330$ km.

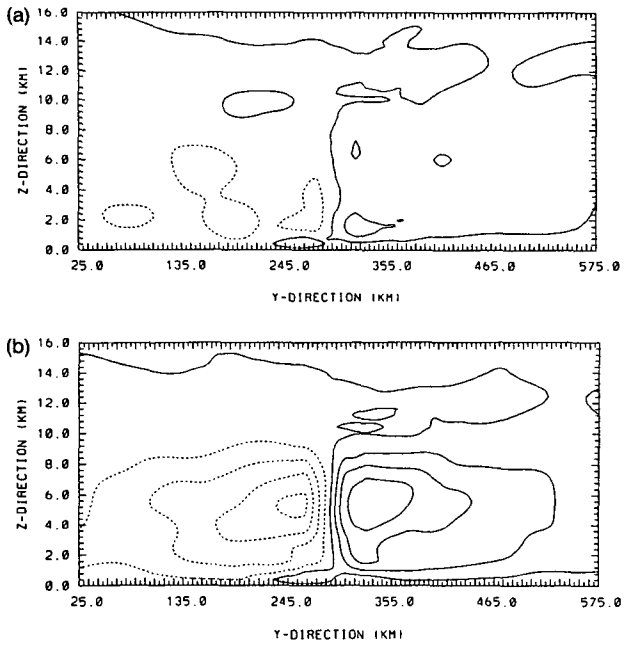

FIG. 10. Time-averaged circulation streamfunction for hours (a) 5–6 and (b) 7–8 for the BCF simulation. Contour interval of 1000 kg m^{-1} s^{-1} for both plots, starting at (a) −500 and (b) −3500 kg m^{-1} s^{-1}. Negative values are dashed. Minimum values: (a) −637, (b) −3764; maxima: (a) 1636, (b) 4279. Because a horizontal space averaging of 40 km is applied to the raw values, the outermost portions of the domain are excluded from the analyses.

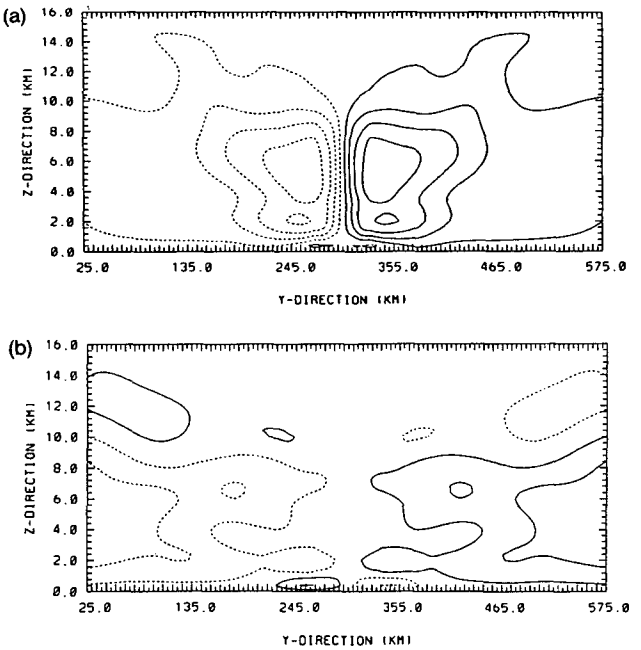

FIG. 11. Time-averaged circulation streamfunction for hours (a) 5–6 and (b) 7–8 for the BTNF simulation. Contour interval of 1000 kg m^{-1} s^{-1} for both plots, starting at (a) −500 and (b) −3500 kg m^{-1} s^{-1}. Negative values are dashed. Minimum values: (a) −637, (b) −3764; maxima: (a) 1636, (b) 4279.

disagree with this hypothesis.) The mesoscale breakdown in the BTNF circulation is more likely a combination of two factors: (i) the larger Rossby radius for the circulation allows its circulation to expand to a larger physical scale, and (ii) the amount of work per unit area that its developing circulation must do against the ambient environment is much larger than that in the BCF environment. The above results support the work of Emanuel (1980), who showed that the mesoscale circulation associated with deep convection became stronger as the ambient baroclinicity was increased (symmetric stability reduced). Whether the BCF system would also eventually experience such a marked mesoscale circulation oscillation is unclear. However, the natural scale for the BCF circulation is much smaller (on the order of 300 km), and the symmetric stability is much smaller so that the convective latent heating in the BCF system is more efficient at generating (and maintaining) a (physically smaller) mesoscale circulation.

In summary, the simulated mesoscale/convective system displayed characteristics similar to observed squall line–type MCSs [for a review, see Houze et al. (1989)]. By the last hour, the system became warm core, with high pressure aloft and low pressure at the surface (Figs. 13a,b). The cool-side circulation dominated, with a development of a quasi-balanced positive zonal momentum anomaly (Fig. 13c) downstream of the mesohigh aloft. Multiple updrafts developed as the system slowly propagated toward the warm air. A trailing cloud anvil formed, within which strong horizontal mixing and intermittent turbulence developed.

It is interesting that the development of the positive zonal countercurrent to the north of the negative zonal

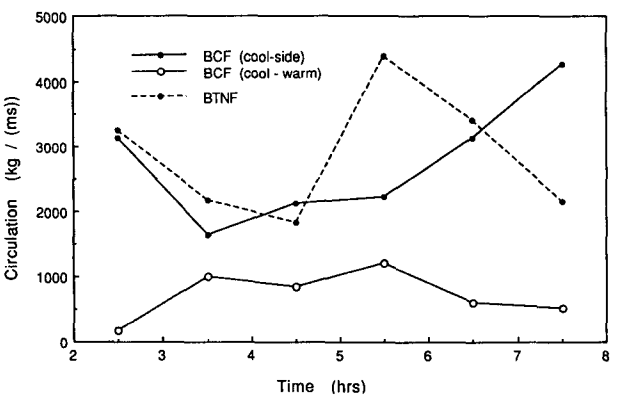

FIG. 12. One-hour time-averaged circulation streamfunction maxima ψ_{max} for the BCF and BTNF simulations. The maxima for the northern half of the respective systems are shown (BCF baroclinically cool side). Also shown are the differences $\psi_{diff} = \psi_{max} - |\psi_{min}|$ between the cool- and warm side for the BCF simulation. The BTNF circulation is a mirror image about the center of the domain ($\psi_{diff} = 0$).

wind anomaly is consistent with Rossby's geostrophic adjustment results [see Blumen (1972) for a review]. Based on Rossby's results, one would also expect a positive zonal countercurrent to the south of the upper-level negative zonal wind anomaly. Although strictly speaking no positive countercurrent developed, the negative u' became somewhat less negative in a wedge on the southern edge of the anomaly (Fig. 13c). Perhaps the vertical momentum transport in the deep convection on the leading edge of the system and the ambient baroclinicity (with a predominantly cool-side circulation) contributed to the reduced strength of this zonal countercurrent.

Two other features, the cool-side meridional outflow jet and rear inflow jet, were not simulated to the strength often observed in real squall-line MCSs. The outflow jet was better simulated, but was still somewhat weaker. The two-dimensionality and/or lack of the ice phase are possible contributing factors.

2) NONLINEAR CONDITIONAL SYMMETRIC INSTABILITY

The following meridional and vertical equations of motion show the essential dynamics for nonlinear conditional symmetric instability:

$$\frac{dv'}{dt} = -fu'_{ag}, \tag{30}$$

$$\frac{dw'}{dt} = -\frac{1}{\bar{\rho}}\frac{\partial p'}{\partial z} + g\frac{\theta'_v}{\bar{\theta}_v}. \tag{31}$$

Here the primed quantities refer to perturbation quantities about a hydrostatic and geostrophic base state, and inviscid flow is assumed.

Although not a complete system, (30) and (31) show that thermal buoyancy accelerates the updraft and ageostrophic zonal momentum anomalies accelerate the meridional outflow. For the base state in this study, a parcel would be accelerated upward and northward toward its equilibrium M surface (Fig. 3). Taken together, this combined buoyant/inertial acceleration is the numerical model equivalent of CSI described by the analytical model in section 3a. Sometimes the phenomenon is referred to as slantwise convection (Emanuel 1983b). In moist adiabatic conditions (classic CSI), both acceleration mechanisms are of comparable importance (Emanuel 1983a), while with CAPE, the Lagrangian parcel model (section 3a) shows that the vertical accelerations are much stronger than those in the horizontal.

In the Lagrangian parcel model approach (section 3a), the perturbation pressure forces are neglected, the buoyancy is parameterized in terms of the base-state stratification, and the perturbation ageostrophic wind is parameterized using conservation of zonal momentum (28) [see also Emanuel (1983a) and section 3a]. It is important to note that no change is allowed in the ambient environment in which the CSI develops; thus, any negative zonal momentum anomalies that would occur in a nonlinear model are assumed to be completely eliminated after a long amount of time (proportional to the inertial time scale).

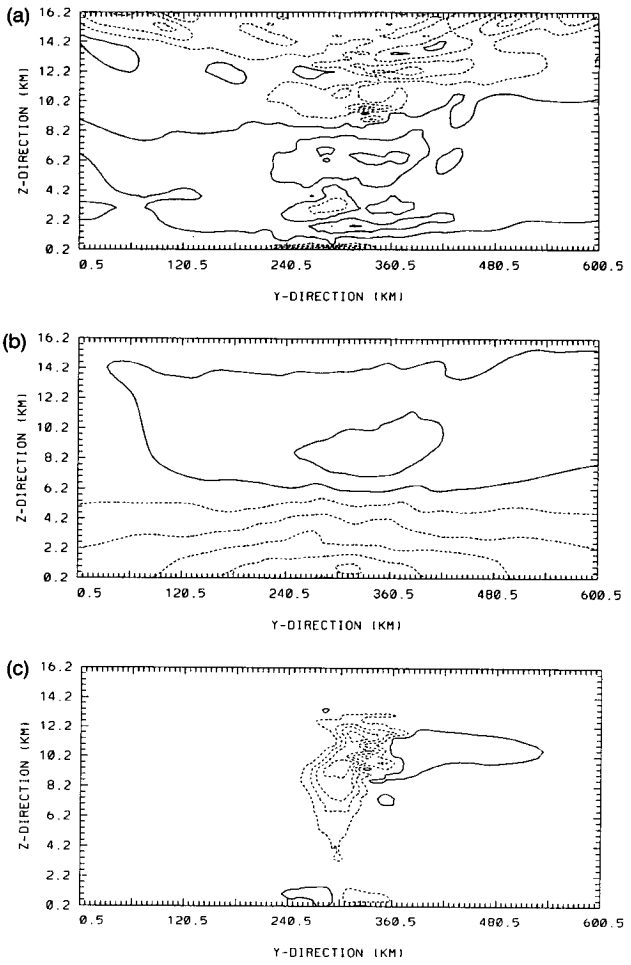

FIG. 13. Time-averaged perturbation (a) potential temperature, (b) pressure, and (c) zonal wind for the BCF simulation for hour 7–8. Horizontal space averaging of 20 km is applied to the raw values. Contour interval of (a) 0.5 K, (b) 0.2 mb, (c) 3 m s^{-1}, starting at (a) −1.25 K, (b) −0.9 mb, and (c) −10.5 m s^{-1}, with negative values dashed. Minimum values: (a) −1.94 K, (b) −0.93 mb, (c) −12.81 m s^{-1}; maxima: (a) 1.52 K, (b) 0.43 mb, (c) 3.33 m s^{-1}.

In the BCF simulation, the above assumption is violated as the negative zonal wind anomaly actually grows with time (Fig. 6). This occurs as rather persistent deep convection in the core and on the leading edge of the system continually transports low-level momentum to the upper levels. The horizontal transports of zonal momentum in the CSI inertial outflows attempt to bring the zonal momentum field back toward its equilibrium configuration. However, the momentum field undergoes geostrophic adjustment and becomes quasi-balanced on mesoscale time scales (compare Fig.

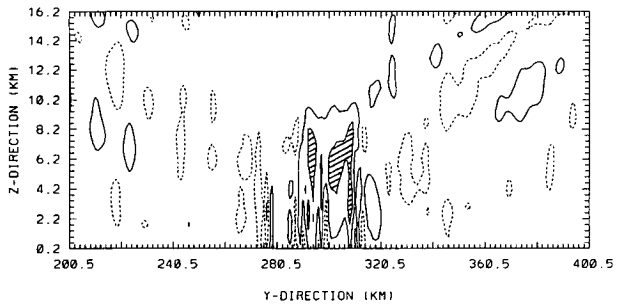

FIG. 14. Changes in vertical wind w' due to ageostrophic mass divergence tendencies (meridional CSI accelerations), over the hours 4–6 for the BCF simulation. Vertical motions obtained from anelastic continuity equation, assuming vanishing vertical motion tendencies at the domain top. Space averaging of 20 km applied to raw values. Contour interval is 0.4 m s^{-1}, starting at -0.6 m s^{-1}. Minimum value: -0.63; maximum: 0.89. Hatched areas indicate increases in vertical motion of greater than 0.6 m s^{-1}. See text for further details.

6 and Fig. 7), and the northward progression of the momentum anomaly is reduced. The nonlinear CSI is thus modified by geostrophic adjustment, which occurs on a time scale similar to the meridional CSI accelerations (30). This balancing helps reduce the potential strength of the meridional outflow, which additionally develops in rather thin layers. Physically, this occurs because the modes of large vertical depth are more efficient in generating adverse meridional pressure gradients (Stevens and Ciesielski 1986).

Further diagnostics show that the nonlinear CSI meridional accelerations implied by (30) are associated with net mass divergence tendencies aloft and vertical motion tendencies via continuity of mass. Figure 14 shows the time-averaged mesoscale meridional and associated vertical motion changes, for hours 4–6, as computed from (30) (the nonlinear terms in the total derivative were included with the ageostrophic term for display purposes). The mesoscale vertical motion changes induced by the meridional CSI accelerations are quasi-periodic in the horizontal (hatched areas in Fig. 16) roughly within the core of the system. Over time, these tendencies have the effect of generating a quasi-periodic vertical motion structure within the system, which helps explain the multiple updraft structure that develops over the last 4 h (Fig. 9).

While the above diagnostic suggests the importance of the upper-level momentum anomalies u' in modulating the convective development in the BCF system, there remains a "chicken and egg" problem. That is, is the horizontal mass divergence in the CSI outflow branch supporting more convection, or is it the other way around? The nonlinearity in the system makes analytical approaches in this area very difficult.

Despite this difficulty, some progress was made in this area through a simple sensitivity experiment with the nonlinear mesoscale/cloud model. Two additional numerical simulations were performed to assess the impact of nonlinear feedbacks of an (initially unbalanced) upper-level zonal momentum anomaly on the system evolution. The simulations were 4 h each on a model domain 300 km wide, and used the same baroclinic environment as for the main BCF simulation. Convection was initiated in both simulations with a warm moist bubble ($\theta'_{max} = 0.5$C) in the center of the domain. BCF_s will refer to the control BCF simulation on the small domain, while BCF'_s refers to the simulation with the initial u' anomaly. The simulations were otherwise identical. The zonal wind field for $t = 0$ in the BCF'_s simulation was obtained from the BCF_s control simulation at 90 minutes into the integration. In essence, the BCF'_s simulation starts out with an upper-level momentum anomaly in addition to the warm bubble.

Figure 15 summarizes the convective activity in the form of a time series displaying the maximum vertical motion for the two simulations. The locations of the convective updrafts vary with time in both of the simulations, with redevelopments generally occurring on the baroclinically warm side of the initial convection. The positive impact of the negative u' anomaly is apparent in the 90 min immediately following the initial convection, with much stronger convective redevelopments in the BCF'_s simulation. Examination of the model output at 1-minute intervals revealed that the meridional outflows from the initial convection remained stronger on the baroclinically cool side over a longer time in the BCF'_s system. These stronger outflows ventilated the upper levels, promoting further convection. This illustrates the complex scale interaction that developed between the convection and the zonal momentum anomaly. The initial convection is nearly identical in both simulations, but on mesoβ time scales the increased mesoscale cool-side outflow in the

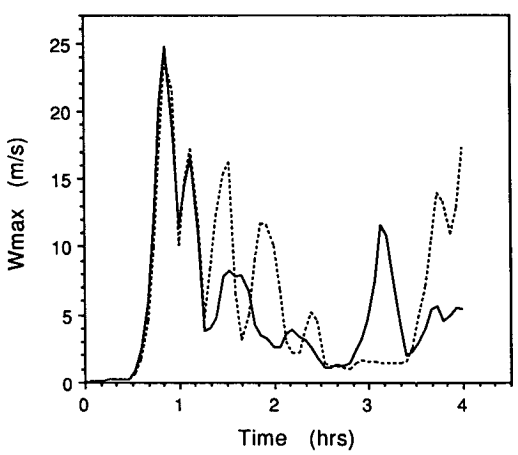

FIG. 15. Time series of the maximum vertical velocity w_{max} for the BCF'_s simulation which contains an initial unbalanced upper-level zonal momentum anomaly (dashed) and the control BCF_s simulation (solid). Locations of individual maximum updrafts become progressively more different with time in the two simulations.

BCF_s' system fosters the development of more convection. Physically, the meridional outflows in the BCF_s' system are less constrained by the relatively weaker upper-level inertial stability in the immediate mesoscale environment of the developing convection, and can remain stronger over time to provide the upper-level support required for subsequent convection.

The differences in the convective redevelopments after hour 3 are more difficult to explain, but appear to be more dependent on the developing mesoscale circulation. More diagnostics would be required, but the longer time required for convective redevelopment in the BCF_s' simulation is consistent with the greater efficiency of the earlier convection at processing the low-level water vapor. Once convection redevelops, it again becomes stronger than that in the control, assisted as before by a more favorable upper-level zonal momentum field. Overall, the BCF_s' system produces 36% more rainfall than the control over the 4-h simulation.

In summary, the simulated nonlinear CSI with CAPE differs from classic CSI in two respects. First, the convective time scale for the vertical momentum transport is much shorter than the inertial time scale for horizontal transport. The consequences of this for the evolution of the system were described above. In classic CSI (no CAPE), the vertical and horizontal transports both occur on an inertial time scale. Second, the vertical fluxes of heat are very large for CSI in a convectively unstable atmosphere. Contrast this to classic CSI, in which the vertical fluxes are much smaller or nonexistent. Based on these distinctions, a new definition of slantwise convection is proposed: the term "slantwise convection" would refer to the sloping convective updraft/cool side outflow that develops with the release of CSI in a convectively unstable atmosphere.

3) Circulation growth

Bennetts and Hoskins (1979) have shown, using a linearized circulation tendency equation for two-dimensional flow, that thermal wind imbalances in the perturbation mass and wind fields give rise to transverse circulations, which attempt to restore the balance. In the present simulation, these imbalances are generated largely by vertical convective transports, while the circulation develops on an inertial time scale as part of the geostrophic adjustment process. In the larger picture, the mesoscale circulation grows (in an upscale manner) from imbalances generated by the deep convection associated with the nonlinear CSI.

Following Bennetts and Hoskins (1979), a linearized, inviscid tendency equation for the x component of vorticity can be derived from (30) and (31) as

$$\frac{\partial \nabla^2 \psi}{\partial t} = f \frac{\partial}{\partial z}(\bar{\rho} u') + g \frac{\partial}{\partial y}\left(\frac{\bar{\rho}}{\bar{\theta}_v}\theta_v'\right), \quad (32)$$

where

$$\nabla^2 \psi = \frac{\partial \bar{\rho} w'}{\partial y} - \frac{\partial \bar{\rho} v'}{\partial z} = \xi$$

is the vorticity, and ψ is the circulation streamfunction. As a simple example, consider a concentrated latent heating source ($\theta_v' > 0$), symmetric about its central maximum. In a nonrotating barotropic atmosphere, opposing mirror-image transverse circulation cells develop about the center of the heat source, with rising motion at the center and subsidence at some distance on either side. Considering next the effects of baroclinicity alone, the same heat source from above would give rise to unequal opposing transverse circulation cells. This occurs because there is a net decrease in the quantity $(\bar{\rho}/\bar{\theta}_v)$ toward the north across the heat source θ_v'. As a result, the baroclinically cool-side circulation tendency would be larger. This circulation tendency is also termed thermally direct in the sense of the base-state thermal structure: the warmer air to the south of the cool-side circulation cell center rises and the cooler air to the north of it sinks. Since a thermally indirect circulation cell develops on the baroclinically warm side of the heating source, the net effect of the concentrated latent heating in the baroclinic atmosphere is to reduce the strength of the ambient baroclinicity. The effect of a localized convectively generated negative momentum anomaly alone also results in a thermally direct circulation tendency directly beneath it, with lifting on its baroclinically warm side and subsidence on the cool side. Qualitatively, then, concentrated latent heating and associated vertical momentum transport would be expected to give rise to a predominantly thermally direct circulation, with mesoscale lifting skewed to the baroclinically warm side of the heat source. Overall, the circulation tendency described above acts to bring the convectively generated momentum field and mass field back toward thermal wind balance: the thermally direct circulation tendency reduces the ambient baroclinicity across the region of reduced vertical wind shear. The reduced shear itself results from the convective momentum transport in the concentrated heating.

The above qualitative arguments were supported in general by the results from the BCF simulation, as the baroclinically cool-side circulation grew faster than that on warm side (Figs. 10, 12). However, there was some variability on mesoscale time scales. For example, in the 4–6-h time frame, the cool side grew faster than the warm side, but thereafter, the warm side grew faster (Fig. 12). The thermal wind imbalance circulation tendencies for the last half of the simulation help explain this behavior (Fig. 16). In the 4–6-h period, the cool-side circulation tendency dominates, and the cool-side circulation grows relatively more quickly during that time. After this, however, the warm-side circulation tendency is larger, and correspondingly, the

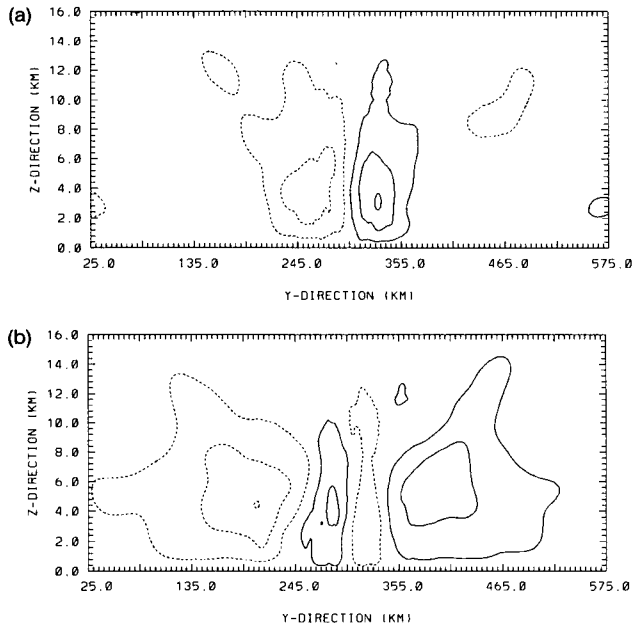

FIG. 16. Time-averaged thermal wind imbalance circulation accelerations for the BCF simulation, in units of kg m^{-1} s^{-1} per hour, for hours (a) 4–6 and (b) 6–8. Horizontal space averaging of 40 km is applied to the raw circulation acceleration values. Contour interval of 1000 kg m^{-1} s^{-1}, starting at (a) −1500 and (b) −2500 kg m^{-1} s^{-1}. Minimum values: (a) −1936, (b) −2521; maxima: (a) 2613, (b) 2248. A value of 1000, for example, means that the circulation would accelerate by 2000 kg m^{-1} s^{-1} over a 2-h period, if no other physical processes acted to decelerate the circulation.

warm-side circulation grows relative to that on the cool side (Fig. 10).

Taken together, the warm- and cool-side tendencies are acting to bring more moisture in at low levels and to ventilate the upper levels. Overall, this is a signature of a positive feedback in that the developing circulation provides a favorable environment for more deep convection in the region of previous convection. More thermal wind imbalances are generated in the core of the system, reinforcing the existing circulation via (32); this helps explain the near-exponential circulation growth over the last 5 h of the simulation. Equation (32) also shows how the geostrophic adjustment process provides the upscale "link" between the convection and larger circulation. Relatively robust convectively generated momentum anomalies associated with the slantwise convection appear to be of primary importance in explaining this complex scale interaction. It should also be noted that the slantwise convection circulation growth mechanism would be more effective in a favorable environment. It is hypothesized that deep low-level moisture and weak ambient symmetric stability were also important in the simulated upscale circulation growth. With deep moisture, the developing mesoscale circulation would be more efficient at generating additional convection. Additionally, a comparison of the BCF and BTNF shows that with weaker ambient symmetric stability, a given amount of latent heat release can generate a more vigorous mesoscale circulation.

4. Summary and conclusions

This study focused on the conditional symmetric instability (CSI) problem (Bennetts and Hoskins 1979; Emanuel 1983a; Xu 1986) in which convective available potential energy (CAPE) exists in the rotating baroclinic atmosphere. The main tool for this investigation was a two-dimensional (y, z) nonlinear, nonhydrostatic numerical mesoscale cloud model. Using an initial value problem approach, this model was used to study the finite-amplitude behavior of CSI, including the effects of explicit convective momentum transport. As part of the analysis, an analytical Lagrangian parcel model with CAPE was developed to help interpret the results from the rotating baroclinic (BCF) simulation. Additionally, a companion nonrotating barotropic (BTNF) simulation was performed to assess the overall impact of baroclinicity on the developing mesoscale circulation. A single warm moist bubble initiated the deep convection in the center of the domain for both simulations.

Two idealized initial atmospheres were developed for the simulations; one was baroclinic, the other barotropic. The baroclinic atmosphere was patterned after precedent conditions taken from a recent case study of mesoscale/convective organization in the presence of weak symmetric stability (Jascourt et al. 1988). This idealized baroclinic atmosphere was initially in thermal wind balance and featured a wind profile $U(z)$ with linear shear in the troposphere (20 m s^{-1}/10 km) and reverse shear above a model tropopause (located at 15 km). The midtropospheric symmetric stability parameter, S, was about 32.5, while the CAPE was about 2400 J kg^{-1}. The initial barotropic atmosphere contained the same wind profile and center-domain sounding (CAPE) as the baroclinic; however since it was nonrotating, no baroclinicity existed and the wind shear was not in thermal wind balance.

Diagnostics performed on the output of the BCF simulation revealed a very intricate life cycle for the mesoscale/convective system characterized by a series of discrete convective events within a growing mesoscale circulation. By 8 h, the circulation had grown upscale with features characteristic of a squall line–type MCS (Houze et al. 1989). Overall, the baroclinically cool-side mesoscale circulation dominated, as predicted by the Lagrangian parcel model of CSI with CAPE. The system became warm core, with mesohigh pressure aloft and mesolow pressure at the surface, and developed multiple mesoscale updrafts as it slowly propagated toward the warm air. Significant vertical transport of zonal momentum occurred within the mesoscale convection, generating (local) subgeostrophic zonal

momentum anomalies aloft with a disruption of thermal wind balance. Over time, geostrophic adjustment acted to balance these anomalies, resulting in a rather large quasi-balanced negative zonal momentum anomaly by the end of the simulation (8 h). A local mesohigh developed downstream of the negative zonal momentum anomaly (on the baroclinically cool side), with a positive zonal momentum anomaly further downstream from it.

Circulation tendency diagnostics showed that thermal wind imbalances, generated by the convection, could help explain the growth of the BCF mesoscale circulation. Ageostrophic wind diagnostics also revealed a nonlinear CSI effect in the simulation, via inertial forces acting on the convectively generated (subgeostrophic) zonal momentum anomalies aloft. Inertially driven mesoscale convective outflows helped ventilate the upper levels of the system on mesoβ time scales, assisting in initiating new convection and increasing the strength and longevity of the developing convection. These CSI meridional outflow accelerations were modulated by geostrophic adjustment.

The main findings of this study may be categorized in terms of the two-dimensional Lagrangian parcel model, and the BCF and BTNF nonlinear numerical simulations.

(i) From the parcel model:

- The addition of CAPE in the Lagrangian parcel model of conditional symmetric instability results in more vertical updrafts and higher growth rates than under moist-adiabatic conditions. For the initial environment used in this study, the updrafts are nearly vertical, with an updraft angle of about 89.8° above the horizontal. This is much more vertical than the more slanted updrafts (45° angle) under moist-adiabatic conditions found by Emanuel (1983a). As in the moist-adiabatic case, the quasi-horizontal outflow branch develops on the baroclinically cool side of the updraft, so that the cool-side mesoscale circulation is predicted to dominate. The growth rate with (large) CAPE was found to be about 18 times larger than that for the moist-adiabatic case. However, this should be viewed with caution since the absence of turbulent mixing and perturbation pressure forces in the parcel model would be more critical in the case with CAPE.

(ii) From the BCF nonlinear numerical simulation, diagnostics showed that a nonlinear CSI developed in response to momentum transport in the deep convection:

- Vertical momentum transport in the deep convection generated an upper-level subgeostrophic momentum anomaly, which because of its small dynamical scale remained relatively robust on mesoscale time scales, enabling the horizontal outflow branch of the nonlinear CSI to develop. In simplest terms, this momentum anomaly formed as a consequence of angular momentum conservation (which occurs in the parcel model as well). The vertical momentum transport occurred on a convective time scale, which disrupted the thermal wind balance.
- The horizontal outflow branch of the nonlinear CSI developed due to imbalances in the pressure gradient and Coriolis forces in the subgeostrophic outflow. Northward accelerations resulted in a net meridional outflow from the core of the system toward the baroclinically cool side. These accelerations were modulated by geostrophic adjustment that acted to balance the zonal momentum anomalies. The simulated outflow was reduced to about 50% of that predicted by the Lagrangian parcel model. Nonetheless, mass transports in the horizontal outflow ventilated the upper levels of the system, thereby helping support further convection.

Circulation diagnostics showed that:

- Development of the circulation could be qualitatively understood using a linearized thermal wind imbalance circulation tendency equation. This diagnostic showed that thermal wind imbalances in the perturbation mass and momentum fields, generated by mass and momentum transports in the deep convection, gave rise to a circulation to bring the perturbed fields back toward thermal wind balance. Overall, the mesoscale circulation developed in an upscale manner, fostered by latent heat release in the rather persistent convection. Near-exponential growth of the cool-side circulation maxima was diagnosed over the last 5 h of the simulation. Deep low-level moisture and weak ambient symmetric stability are hypothesized to be important factors in this simulated mesoscale growth.

(iii) A comparison of the BCF and BTNF numerical simulations showed that, overall, baroclinicity enhanced the mesoscale circulation growth and was associated with larger amounts of precipitation. The BTNF circulation was more transient (in space and time) than that of the BCF. These results are consistent with the work of Emanuel (1980) and Xu (1986).

For the BCF simulation, the Lagrangian parcel model theory was useful for predicting that the baroclinically cool-side circulation would dominate. The mesoscale updrafts were simulated at an angle of approximately 70° from the horizontal, which was shallower than the 89° angle predicted by the parcel theory. Physical processes such as turbulence and water loading (not present in the parcel model) may be important in explaining the difference.

The nonlinear CSI simulated here with CAPE differed from classic CSI (no CAPE) in two respects. First, with CAPE, vertical momentum transports occurred on a convective time scale, while the horizontal momentum transports occurred on an inertial time scale. In classic CSI (no CAPE), vertical and horizon-

tal transports both occur on an inertial time scale. Second, large vertical heat fluxes occurred in the present simulation, which contrasts with classic CSI in which the vertical fluxes are small or nonexistent. The vertical heat flux enabled convective momentum transport across isentropic surfaces, giving rise to the nonlinear CSI via formation of a subgeostrophic momentum anomaly aloft. Based on these distinctions, a new definition of slantwise convection is proposed: "slantwise convection" would refer to the sloping convective updraft/cool side outflow that develops with the release of CSI in a convectively unstable atmosphere.

Acknowledgments. I would like to extend my appreciation and thanks to my advisor, Professor David D. Houghton, for his support throughout this study. His scientific guidance provided many excellent suggestions to improve this work. Special thanks are also extended to Professors Donald R. Johnson, Gregory J. Tripoli, and John A. Young. Discussions with Professor Kerry A. Emanuel and the comments of the anonymous reviewers were excellent and helped make this a much better paper.

I am thankful to Professor Jerry Straka for providing the initial numerical cloud model and microphysics codes that were used to construct the mesoscale cloud model needed for this study. The use of Professor John R. Anderson's computer resources during the model development and testing phases is also greatly appreciated.

The research in this paper was supported by the National Science Foundation under Grants ATM-85-14730 and ATM-9111597. The numerical computations were made using a CRAY XMP-48 computer at the National Center for Atmospheric Research (NCAR), with Grant 35381046 from the NCAR Scientific Computing Division.

APPENDIX

Cloud Microphysics

The explicit water cycle is adapted from the work of Lin et al. (1983). The microphysics processes are given by

$$M_\theta = -\beta(\mathrm{CN} + E_R) \tag{A1}$$

$$M_{qv} = \mathrm{CN} + E_R \tag{A2}$$

$$M_{qc} = -\mathrm{CN} - A_R - C_R \tag{A3}$$

$$M_{qr} = A_R + C_R - E_R + F_R, \tag{A4}$$

where $\beta = L_v/(C_p\bar{\Pi})$ and $\bar{\Pi} = (\bar{p}/p_{00})^\kappa$. The latent heat of vaporization $L_v = 2.5 \times 10^6$ J kg^{-1}, with $C_p = 1004$ J kg^{-1} K^{-1}, $p_{00} = 10^5$ Pa, and $\kappa = R_d/C_p$, where $R_d = 287$ J kg^{-1} K^{-1}. The above conversions are defined as

- CN condensation of water vapor/evaporation of cloud drops (dq_{vs}/dt): q_v to q_c/q_c to q_v (via saturation adjustment to the saturation mixing ratio q_{vs})
- A_R autoconversion, cloud drops to raindrops: q_c to q_r
- C_R collection of q_c by q_r
- E_R evaporation of rainwater: q_r to q_v
- F_R $1/\bar{\rho}\,\partial(\bar{\rho}q_rV_{tr})/\partial z$ (Rainwater fallout), and
- V_{tr} terminal fall speed of rainwater (given in Table A1).

Condensation/evaporation is determined via the saturation adjustment procedure of Soong and Ogura (1973), which is implemented in the numerical model as described by Klemp and Wilhelmson (1978). Teten's formula for the saturation vapor pressure is used to determine areas requiring saturation adjustment:

$$q_{vs} = \frac{3.8}{\bar{p}} \exp\left(17.2693882\,\frac{\bar{\Pi}\theta - 273.16}{\bar{\Pi}\theta - 35.86}\right). \tag{A5}$$

The overbars refer to base-state quantities; use of the base-state pressure (units: mb) follows the convention of Klemp and Wilhelmson (1978) and Wilhelmson and Ogura (1972).

The microphysics conversion rates are given by

$$A_R = \bar{\rho}(q_c - q_{c0})^2 \times \left(1.2 \times 10^{-4} + \frac{1.569 \times 10^{-12}N_1}{D_0\bar{\rho}(q_c - q_{c0})}\right)^{-1} \tag{A6}$$

$$C_R = \frac{\pi E_C \eta_{OR} a\Gamma(3+b)q_c}{4\lambda_R^{3+b}}\left(\frac{\rho_0}{\bar{\rho}}\right)^{1/2} \tag{A7}$$

and

$$E_R = \frac{2\pi(S-1)\eta_{OR}}{\bar{\rho}} \frac{\left(0.78\lambda_R^{-2} + 0.31S_c^{1/3}a^{1/2}\Gamma[(5+b)/2]\left(\frac{\rho_0}{\bar{\rho}}\right)^{1/4}\nu^{-1/2}\lambda_R^{-(5+b)/2}\right)}{\left(\frac{L_v^2}{K_aR_vT^2} + \frac{1}{\bar{\rho}q_{vs}\psi}\right)}. \tag{A8}$$

The autoconversion to rainwater depends on N_1 (=1000, the number concentration of cloud droplets in the assumed Marshall–Palmer distribution) and D_0 (=0.15, the dispersion), and does not occur until the

TABLE A1.

Symbol	Description	Value	Units
a	Constant in empirical formula for V_{tr}	2115	$cm^{1-b}\ s^{-1}$
b	Constant in empirical formula for V_{tr}	0.8	
CN	Condensation/evaporation for water vapor		$g\ g^{-1}\ s^{-1}$
C_P	Specific heat of air at constant pressure	1004	$J\ kg^{-1}\ K^{-1}$
C_R	Collection rate of cloud water by rainwater		$g\ g^{-1}\ s^{-1}$
C_v	Specific heat of air at constant volume	717	$J\ kg^{-1}\ K^{-1}$
D_0	Dispersion of the condensation-produced droplet size spectrum	0.15	
E_c	Collection efficiency of rain	1.0	
E_R	Evaporation rate of rainwater		$g\ g^{-1}\ s^{-1}$
K_a	Thermal conductivity of air	2.4×10^{-2}	$J\ m^{-1}\ s^{-1}\ K^{-1}$
L_v	Latent heat of condensation for water vapor	2.5×10^{6}	$J\ kg^{-1}$
N_1	Number concentration of cloud droplets produced by condensation	1000	cm^{-3}
p_{00}	Reference air pressure	1×10^{5}	Pa
q_c	Cloud water mixing ratio		$g\ g^{-1}$
q_{c0}	Autoconversion threshold cloud water mixing ratio	2×10^{-3}	$g\ g^{-1}$
q_r	Rain water mixing ratio		$g\ g^{-1}$
q_v	Water vapor mixing ratio		$g\ g^{-1}$
q_{vs}	Saturation water vapor mixing ratio		$g\ g^{-1}$
R_d	Specific gas constant for dry air	287	$J\ kg^{-1}\ K^{-1}$
R_v	Specific gas constant for water vapor	461.5	$J\ kg^{-1}\ K^{-1}$
S	Saturation ratio (q_v/q_{vs})		
S_c	Schmidt number (ν/ψ)		
T	Air temperature		K
V_{tr}	Rainwater terminal fallspeed $V_{tr} = \frac{0.01}{6} a\Gamma(4.8)\left(\frac{\rho_0}{\bar{\rho}}\right)^{1/2} \lambda_R^{-0.8}$		$m\ s^{-1}$
β	Heating coefficient ($L_v/(C_p\bar{\Pi})$)		
$\Gamma(\ )$	Gamma function		
γ	Expansion ratio of air (C_p/C_v)	1.4	
η_{OR}	Number of raindrops per unit diameter	0.08	cm^{-4}
κ	Adiabatic constant (R_d/C_p)	0.285 . . .	
λ_R	Parameter in rain distribution $\lambda_R = \left(\frac{\bar{\rho} q_r}{1000\eta_{OR}\pi}\right)^{-1/4}$		cm^{-1}
ν	Kinematic viscosity of air $\nu = (1.718 + 0.0052\bar{T})/1 \times 10^{4}$		$m^2\ s^{-1}$
Π	Exner function for pressure $\bar{\Pi} = (\bar{p}/p_{00})^{\kappa}$		
π	Geometric constant	3.14 . . .	
ρ	Air density (moist)		$kg\ m^{-3}$
ρ_0	Reference (surface) air density		$kg\ m^{-3}$
ψ	Diffusivity of water vapor in air $\psi = 0.226\left(\frac{\bar{P}_0}{\bar{P}}\right)\left(\frac{\bar{T}}{273.16}\right)^{1.81}$		$cm^2\ s^{-1}$

cloud water reaches a threshold amount (q_{c0} = 2 g kg^{-1}, as done by Lin et al. 1983). McCarthy (1974) has observed that cloud water contents of a few grams per cubic meter exist without radar echoes in tropical clouds, so the threshold in (A6) results in more realistic simulation of first echoes (Lin et al. 1983). Collection of cloud water by falling rain (A2) is proportional to the amount of cloud water present and the collection efficiency, E_c, here assumed to be 1. Evaporation of rain is allowed only in unsaturated air ($S < 1$, where $S = q_v/q_{vs}$). A table of microphysics variable and parameter definitions is given in Table A1.

REFERENCES

Anderson, J. R., K. K. Droegemeier, and R. B. Wilhelmson, 1985: Simulation of the thunderstorm subcloud environment. Preprints, *14th Conf. on Severe Local Storms,* Indianapolis, Amer. Meteor. Soc., 147–150.

Asselin, R., 1972: Frequency filter for time integrations. *Mon. Wea. Rev.*, **100,** 487–490.

Barwell, B., and R. Bromley, 1988: The adjustment of numerical weather prediction models to initial perturbations. *Quart. J. Roy. Meteor. Soc.*, **114,** 665–684.

Blumen, W., 1972: Geostrophic adjustment. *Rev. Geophys. Space Phys.*, **10,** 485–528.

Bennetts, D. A., and B. J. Hoskins, 1979: Conditional symmetric instability—a possible explanation for frontal rainbands. *Quart. J. Roy. Meteor. Soc.*, **105,** 945–962.

Clark, T. L., 1977: A small-scale dynamic model using a terrain-following coordinate transformation. *J. Comput. Phys.*, **24,** 186–215.

Droegemeier, K. K., and R. B. Wilhelmson, 1987: Numerical simulation of thunderstorm outflow dynamics. Part I: Outflow sensitivity experiments and turbulence dynamics. *J. Atmos. Sci.*, **44,** 1180–1210.

Durran, D. R., and J. B. Klemp, 1983: A compressible model for the simulation of moist mountain waves. *Mon. Wea. Rev.*, **111,** 2341–2361.

Emanuel, K. A., 1980: Forced and free mesoscale motions in the atmosphere. In "Collection of lecture notes on dynamics of mesometeorological disturbances." CIMMS Symposium, University of Oklahoma/NOAA, Norman, OK, 189–259.

——, 1982: Inertial instability and mesoscale convective systems. Part II: Symmetric CISK in a baroclinic flow. *J. Atmos. Sci.*, **39,** 1080–1097.

——, 1983a: The Lagrangian parcel dynamics of moist symmetric instability. *J. Atmos. Sci.*, **40,** 2368–2376.

——, 1983b: On assessing local conditional symmetric instability from atmospheric soundings. *Mon. Wea. Rev.*, **111,** 2016–2033.

Fovell, R. G., 1991: Influence of the Coriolis force on a two-dimensional model storms. *Mon. Wea. Rev.*, **119,** 603–630.

Hill, G. E., 1974: Factors controlling the size and spacing of cumulus clouds as revealed by numerical experiments. *J. Atmos. Sci.*, **31,** 646–673.

Houghton, D. D., and J. A. Young, 1970: A note on inertial instability. *Tellus,* **22,** 581–583.

Houze, R. A., S. A. Rutledge, M. I. Biggerstaff, and B. F. Smull, 1989: Interpretation of Doppler weather radar displays of midlatitude mesoscale convective systems. *Bull. Amer. Meteor. Soc.*, **70,** 608–619.

Jascourt, S. D., S. S. Lindstrom, C. J. Seman, and D. D. Houghton, 1988: An observation of banded convective development in the presence of weak symmetric stability. *Mon. Wea. Rev.*, **116,** 176–191.

Klemp, J. B., and R. B. Wilhelmson, 1978: The simulation of three-dimensional convective storm dynamics. *J. Atmos. Sci.*, **35,** 1070–1096.

Lilly, D. K., 1965: On the computational stability of numerical simulations of time-dependent nonlinear geophysical fluid dynamics problems. *Mon. Wea. Rev.*, **93,** 11–26.

Lin, Y.-H., R. D. Farley, and H. D. Orville, 1983: Bulk parameterization of the snow field in a cloud model. *J. Climate Appl. Meteor.*, **22,** 1065–1092.

Maddox, R. A., 1983: Large-scale meteorological conditions associated with midlatitude, mesoscale convective complexes. *Mon. Wea. Rev.*, **111,** 1475–1493.

Matsumoto, S., 1961: A note on geostrophic adjustment and gravity wave in the atmosphere. *J. Meteor. Soc. Japan,* **39,** 18–28.

McCarthy, J., 1974: Field verification of the relationship between entrainment rate and cumulus cloud diameter. *J. Atmos. Sci.*, **31,** 1028–1039.

Moncrieff, M. W., and M. J. Miller, 1976: The dynamics and simulation of tropical cumulonimbus and squall lines. *Quart. J. Roy. Meteor. Soc.*, **102,** 373–394.

Nehrkorn, T., 1986: Wave–CISK in a baroclinic basic state. *J. Atmos. Sci.*, **43,** 2773–2791.

Newton, C. W., 1950: Structure and mechanism of the pre-frontal squall line. *J. Meteor.*, **7,** 210–222.

Robert, A. J., 1966: The integration of a low order spectral form of the primitive meteorological equations. *J. Meteor. Soc. Japan,* **44,** 237–245.

Rotunno, R., J. B. Klemp, and M. L. Weisman, 1988: A theory for strong, long-lived squall lines. *J. Atmos. Sci.*, **45,** 463–485.

Schubert, W. H., J. J. Hack, P. L. Silva Dias, and S. R. Fulton, 1980: Geostrophic adjustment in an axisymmetric vortex. *J. Atmos. Sci.*, **42,** 2207–2219.

Seman, C. J., 1991: Numerical study of nonlinear convective-symmetric instability in a rotating baroclinic atmosphere. Ph.D. thesis, 185 pp. [Available from University of Wisconsin—Madison, Dept. of Atmospheric and Oceanic Sciences, Madison, WI, 53706.]

Soong, S. T., and Y. Ogura, 1973: A comparison between axisymmetric and slab-symmetric cumulus cloud models. *J. Atmos. Sci.*, **30,** 879–893.

Stevens, D. E., and P. E. Ciesielski, 1986: Inertial instability of horizontally sheared flow away from the equator. *J. Atmos. Sci.*, **43,** 2845–2856.

Sun, W.-Y., 1984: Rainbands and symmetric instability. *J. Atmos. Sci.*, **41,** 3412–3426.

Thorpe, A. J., and R. Rotunno, 1989: Nonlinear aspects of symmetric instability. *J. Atmos. Sci.*, **46,** 1285–1299.

——, M. J. Miller, and M. W. Moncrieff, 1982: Two-dimensional convection in non-constant shear: A model of mid-latitude squall lines. *Quart. J. Roy. Meteor. Soc.*, **108,** 739–762.

Wilhelmson, R. B., and Y. Ogura, 1972: The pressure perturbation and the numerical modeling of a cloud. *J. Atmos. Sci.*, **29,** 1295–1307.

——, and C.-S. Chen, 1982: A simulation of the development of successive cells along a cold outflow boundary. *J. Atmos. Sci.*, **39,** 1466–1483.

Xu, Q., 1986: Conditional symmetric instability and mesoscale rainbands. *Quart. J. R. Meteor. Soc.*, **112,** 315–334.